Review Article

Syed Irfan*, Sadaf Bashir Khan*, and Zhiyuan Yang

Revolutionizing energy harvesting: A comprehensive review of thermoelectric devices

https://doi.org/10.1515/rams-2024-0023 received November 29, 2023; accepted April 19, 2024

Abstract: The necessity for a shift to alternative forms of energy is highlighted by both approaching consequences of climate change and limited availability of fossil fuels. While a large portion of energy required can be generated by solar and wind, a diverse, sustainable energy generation mix is still necessary to meet our energy needs. By capturing otherwise lost heat energy and turning it into valuable electrical energy, thermoelectric can play a significant part in this. Using the Seebeck effect, thermoelectric generators (TEG) have established their capability to transform thermal energy into electrical energy directly. Furthermore, because they do not include chemical compounds, they are silent in operation and can be built on various substrates, including silicon, polymers, and ceramics. Moreover, thermoelectric generators have a long operational lifetime, are position independent, and may be integrated into bulky, flexible devices. However, the low conversion efficiency of TEG has confined their broad application, hampering them to an academic subject. Until now, recent developments in thermoelectric generators and devices are presuming the technology to catch its place among state-of-the-art energy conversion systems. This review presents the commonly used methods for producing thermoelectric modules (TEMs) and the materials currently studied for TEMs in bulk and printed thermoelectric devices.

Zhiyuan Yang: State Key Laboratory of Environment-friendly Energy Materials, Southwest University of Science and Technology, Mianyang, 621010, China

Keywords: thermoelectric generators, thermoelectric modules, nanoparticles, thermoelectric devices, Seebeck coefficient

1 Introduction

Seebeck made the initial discovery of the thermoelectric phenomena in 1821. By heating the connection between two separate electrical conductors, he demonstrated how to create an electromotive force. It is discovered that the meter registers a minor voltage when the connection between the wires is heated. It has been determined that the size of the thermoelectric voltage is proportional to the difference in temperature between the connections to the meter and the thermocouple junction. The second of the thermoelectric effects was noticed by French watchmaker Peltier 13 years after Seebeck made his discovery. He discovered that depending on the direction of the electric current, passing through a thermocouple results in a minor heating or cooling impact. Since the Joule heating effect always accompanies the Peltier effect, it is very challenging to show the Peltier effect using metallic thermocouples. Showing less heating when the current is transmitted in one way instead of the other is often all that can be done. The Peltier effect may be theoretically illustrated using the setup in Figure 1 by exchanging the meter for a direct current source and mounting a tiny thermometer on the thermocouple junction. The thermoelectric (TE) is explained using the aforementioned phenomena [1-3]. These three phenomena and Joule effect provide the physical foundation for TE transformation procedures [4]. Seebeck observed a magnetic field surrounding the two distinct metal wires in a loop when he warmed up one connection but kept the other at a low temperature (Figure 1(a) and (b)). The formation of the magnetic field due to the temperature difference between two junctions was named thermo-magnetism.

A further explanation was offered by Oersted, whose experiment showed that the magnetic field near the circuit was unaffected by the temperature change. The temperature variation produced a voltage $V_{\rm ab}$ and an electric current in the circuit, which produced the experiment's

^{*} Corresponding author: Sadaf Bashir Khan, School of Manufacturing Science and Engineering, Key Laboratory of Testing Technology for Manufacturing Process, Ministry of Education, Southwest University of Science and Technology, Mianyang 621010, China, e-mail: sadafbashirkhan@swust.edu.cn

^{*} Corresponding author: Syed Irfan, State Key Laboratory of Environment-friendly Energy Materials, Southwest University of Science and Technology, Mianyang, 621010, China, e-mail: syedirfan@swust.edu.cn

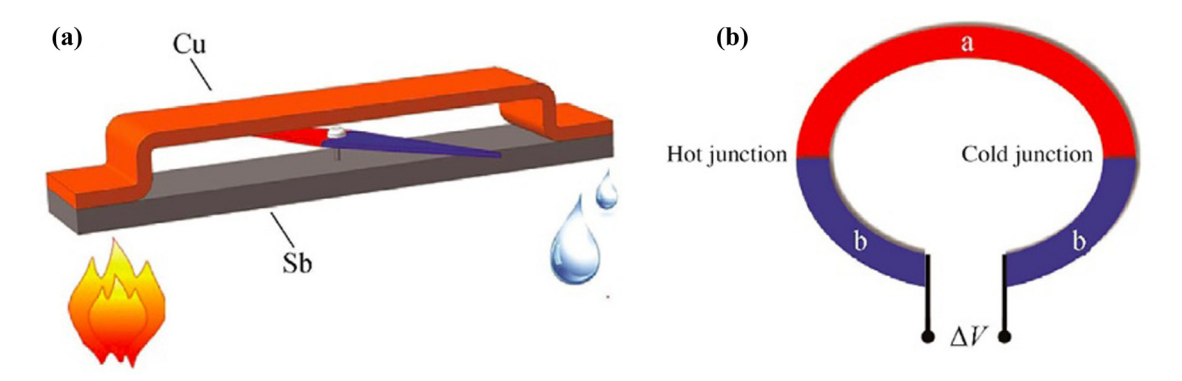


Figure 1: (a) Experimental observation and (b) seebeck effect, reproduced with the permission of Chen et al. [5].

magnetism. The formation of electric current due to the temperature difference was named thermoelectricity [6]. Seebeck first identified the phenomenon; since then, it has been referred to as the Seebeck (Sb). The Seebeck effect, which explains the phenomenon of the carrier's directly pumping heat, is the reverse of the Peltier effect. Additional heat will be released or absorbed at these two junctions in addition to the Joule heat created when a current is applied to a circuit of two conductors. Since J. C. A. Peltier, a French physicist, first identified this effect in 1834, it has been named after him.

He connected the Bi and Sb wires and observed how a metal connection caused water droplets to condense when an electric current was sent across the circuit. When the current turned around, the ice disintegrated (Figure 2a). When electric current applied at junction of two different Fermi-level conductors, the electrons will either jump from the high to the low or in the opposite direction across the

interface potential barrier [7]. They will absorb or release energy in the form of heat at the junction (Figure 2b). It was not until 1855 that William Thomson (Lord Kelvin) recognized this issue as being related to the link between the Seebeck and Peltier effects [8]. He reasoned that there must also be a third effect. In addition to the Joule heat, a uniform conductor should experience reversible heat absorption or release as an electric current passes through it. The Thomson effect was introduced in 1867 after this effect had been empirically verified. Several research works take the constant value of Thomson coefficients and establish that the coefficient showed a significant impression on the efficiency of thermoelectric generators (TEGs). Subsequently, Yamashita et al. [9] investigated the linear temperaturedependent effect of TE materials on TEG performance. The asymptotic solution to the nonfundamental heat control equation for TE materials was proposed by Sandoz-Rosado et al., [10] and the equations were derived from

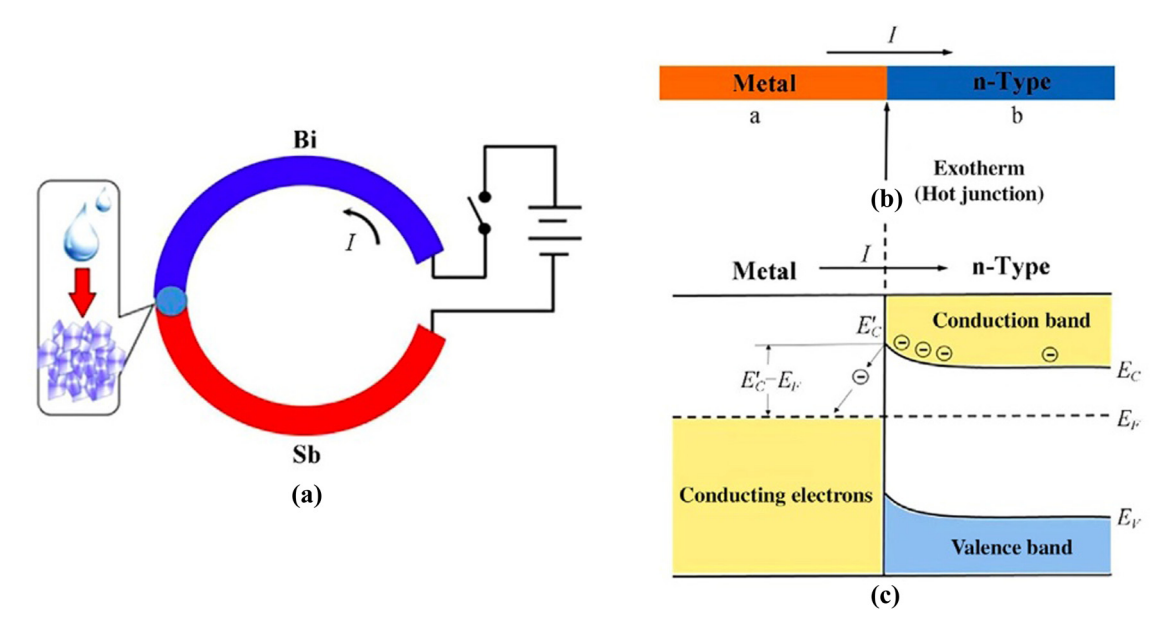


Figure 2: (a-c) The Peltier effect, reproduced with the permission of Chen et al. [5].

the temperature-dependent cumulative model incorporating Thomson's effect by Kim et al. [11].

2 Thermoelectric devices

Thermoelectric devices are like heat engines. Their efficiency constraint is comparable to the Carnot efficiency [12]. According to the Carnot cycle [13], the energy can be absorbed or dumped from a high- or low-temperature reservoir; it cannot be taken from room temperature. Because of the trade-off between efficiency and power that applies to all heat engines, achieving the Carnot efficiency at finite power is complicated. It is noted that without violating the trade-off relation, the Carnot efficiency at finite power might be reached in the vanishing limit of a system's relaxation times. The TEG characteristic and outputs not only depend on the Carnot efficiency but also on the dimensionless parameter of material called a figure of merit (ZT) [14]. This dimensionless parameter depends on numerous material characteristics such as temperature [15], Seebeck coefficient [16], electrical [17], and thermal conductivity [18]. Modern TE device designs, including traditional TE module design, flexible device design, microdevice design, and applications in various sectors, require high-efficiency levels. TE devices for power generation have received significant attention due to their high reliability, solid-state operation, and stability. When designing thermoelectric power generation devices, it is necessary to consider design principles, fabrication techniques and testing methods, interface optimization, barrier laver design, electrode fabrication, protective coatings, and component and module estimation aspects of TE devices. These TE designs depend on elegant, dimensional designs that guarantee excellent stability and performance [19]. Environmental factors that may harm or improve device performance include oxidation, magnet fields, pressure, and radiation.

Usually, the metal-electrode links n- and p-type TE material to form the TE module (element) [20]. TE devices are created by joining many TE modules in series electrically and in parallel thermally due to the low output voltage of a single TE module [21]. The device is usually assembled by soldering a copper electrode to the ceramic sheet with a thermally conductive surface that acts as the electrical insulating board for both the cold and hot ends. A copper sheet is directly adhered to a ceramic substrate using the copper-cladding technique in a preset pattern [22]. The n- and p-type thermoelectric modules (TEMs) are linked using standard soldering methods to fabricate a sandwich structure. The wettability of TE can be improved with the help of Nickel, which can be used in solders and soldering surfaces. Solder alloys are essential for the fabrication of integrated circuits and electronic devices. Nickel solders are popular because of their low melting point, superior solderability, and low price [23]. Despite the simplicity and low cost of this preparation procedure, the use of ceramic leads to brittleness and mechanical stress.

For the construction of thermoelectric devices (TEDs), complex electrode preparation techniques such as arc-spraying [24], high-temperature diffusion welding [25], and a combination with Spark plasma sintering [26] have been adopted. The TE device can work at temperatures that are not constrained by the melting point of the solder when using the arc-spraying technique, which shows outstanding thermal stability [27]. A transition or intermediary layer is often formed on the electrode connection surface of TEMs in the interim to facilitate interface bonding. The arc spraying apparatus also has good mechanical stress resistance because the TEMs are fastened and packed in the gap between the frame and electrode. Recently, a one-step method for producing devices was developed that uses hot pressing or SPS to concurrently make n-type and p-type materials and sinter electrodes [28], barrier [29], and TEMs [30]. Using integrated methods, creating low interface contact resistance and highstrength bonding of TEMs and electrodes is straightforward. TEDs are divided into three types: π -type [31], O-type [32], and Y-type [5], based on their diverse designs [33]. The TE gadget of the π -type is the most well-known of them (Figure 3).

The TE modules in π -type TE devices are housed within two efficient heat-conducting electrically insulated ceramic panels [34]. The heat flow is generally directed to a ceramic flat plate, which is appropriate for a flat source of heat's operational environment [35]. Unidirectional heat flow makes it simple to establish uniform heat flow density in TEMs [36], and the best structure design can enhance the TE performance to achieve high efficiency. However, a TE device frequently constrains cold and hot surfaces. The temperature change caused severe thermal stress and impaired the structure's endurance due to the different thermal expansion of other materials [37]. In an O-type TE device, the columnar heat source alternates coaxially with n- and p-type TEMs [26]. The annular insulation material's layer is positioned in the middle of each layer of TE material to establish electrical isolation between the adjacent layers [38]. In addition, metal coil electrodes are used to connect nearby TEMs. In particular, a radial heat flow is observed in the cylindrical heat source. Therefore, a ringlike TE device is suitable for nonflat heat sources. However, the efficient design of electric fields and temperature makes achieving the radial heat flow and current difficult.

4 — Syed Irfan et al. DE GRUYTER

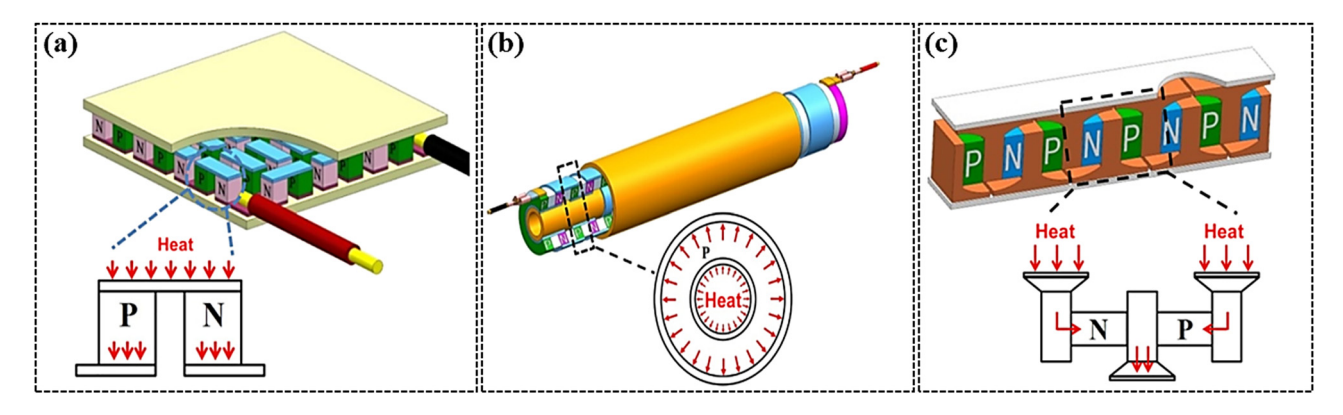


Figure 3: (a) π-shaped TE module, (b) tube-shaped TE module, and (c) Y-shaped TE module, reproduced with the permission of Yubing et al. [34].

Compared to a flat device, welding of specifically shaped TEM, metal electrodes, and device integration is much more complex, and the production cost is significantly higher [26].

In Y-type TED, connecting electrodes contain cylindrical or rectangular n- and p-type TEM. The connection plates of electrodes offer conductive channels for nearby n- and p-type TEM and function as heat-collecting and

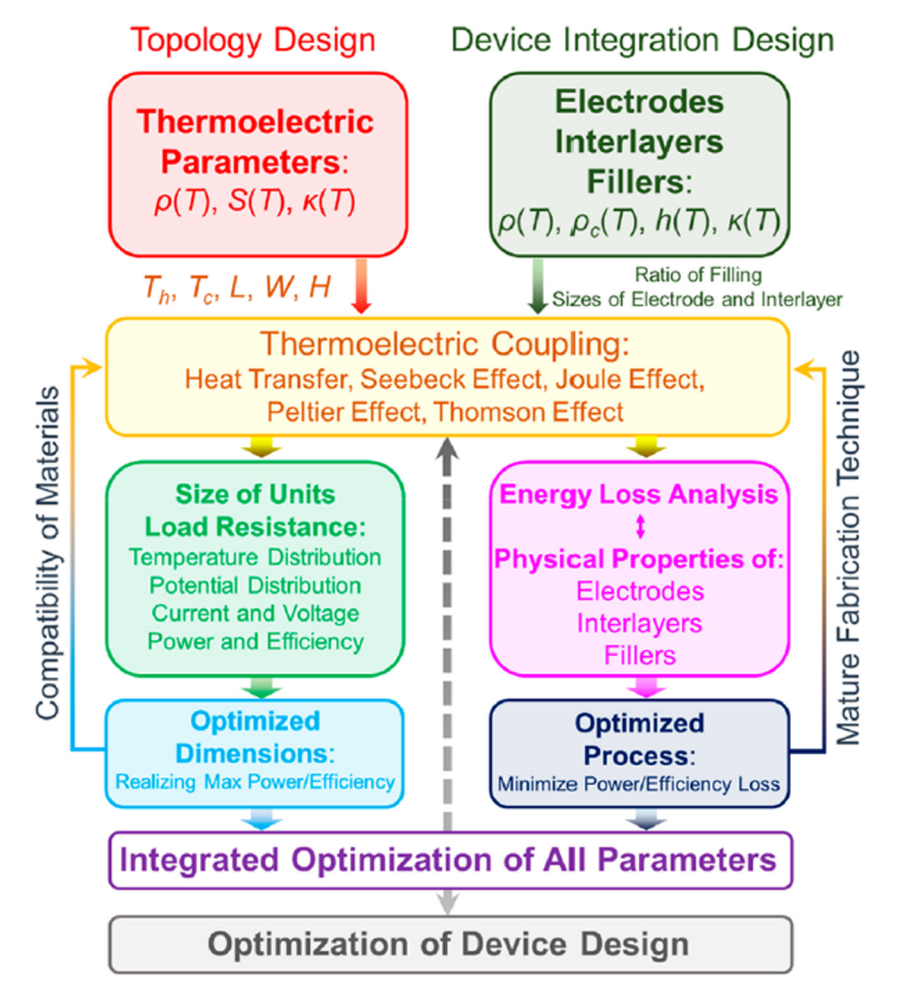


Figure 4: The flowchart description of the basic design criteria for TED, reproduced with the permission of Deepthi [39].

transmission devices [40]. The lateral series thermal expansion of n- and p-type TEM avoids stress concentration due to variations in expansion coefficients and provides better freedom in TEM design parameters [41]. Furthermore, the Y-type construction allows each TE module to be individually optimized structurally [42]. TEM could have a variety of sizes in terms of structure interface and height, which is advantageous in the fabrication of divided structures. The heat and current density nonuniformity flow in Y-shaped TED influenced the efficiency of the TEM materials and shrink device performance [39].

Figure 4 depicts the basic design criteria for TED, which applies to all TED types. The flow diagram shows that the device's topological layout directly impacts output attributes, such as device energy density. As a result, matching the device topologies under real operating conditions is the foundation for optimizing a TE powergenerating system's comprehensive indicators [43]. The limits and affecting elements must be thoroughly studied depending on the operating mode of the TED. In the device design phase, it is critical to incorporate mathematical investigation, thermal-electric structure coupling inquiry, finite element numerical modeling, and transient structure analysis [44]. Several interconnected structural parameters must be optimized simultaneously following the device's overall modeling. The efficiency of TED's energy is affected by the TEM performance and the difference in temperature between the two ends of the materials and by their size [45]. When different resistivity of the p- and n-type TEM composes a TE unit, the performance is reduced, which can be countered by adopting two TE "legs." In general, the finite element approach is beneficial for resolving such problems. When a temperature gradient (ΔT) is introduced, the change carriers (electrons for n-type materials and holes for p-type materials) starts moving from the hot side and diffuse to the cold side, this phenomenon is called material's TE energyharvesting mechanism. An electrostatic potential (ΔV) is consequently created. A solitary n- or p-type TE leg produces an

extremely low electrostatic potential (varying from μV to mV depending upon the situation). TE generators are usually composed of dozens or even hundreds of TE couples to gain high output voltage and power.

Furthermore, a single TEM's ideal working temperature range is frequently small [46]. The efficiency is limited when utilizing a single TEM [47]. Every material has different physical characteristics; therefore, the degree of nonlinearity increases in temperature distribution. In the case of segment TED's, they have many interfaces and complicated topologies, making it challenging to optimize device performance. Another critical component to consider in designing the device is the fill factor (F), which is the ratio of the TEM to the area of the ceramic plate [48]. In general, F must be optimized to maximize efficiency [49]. The link between electrodes and TEM is critical in TED design, particularly for high-temperature electrodes [50]. Because TEDs may remain in service for lengthy durations, interdiffusion and chemical reactions take place at the interfaces of high-temperature electrodes and TEM interfaces [51]. This reduces the efficiency due to increased electrical and thermal resistance. The reasonable remedy for this problem is to place a suitable transition layer between the electrodes and the TEMs, acting as a diffusion barrier [52]. In low temperatures, TED's transition layer's purpose is to increase solder and material's wettability. It also helps reduce thermal and interface resistance. However, its selection and design are much more complicated in the case of high-temperature TEDs [53]. Here is the real example of TEM and TEG in daily life as shown in Figure 5.

3 Nano-particle (Na-Par) preparation methods

In this section, we present some of the commonly used methods for preparing the TEMs.

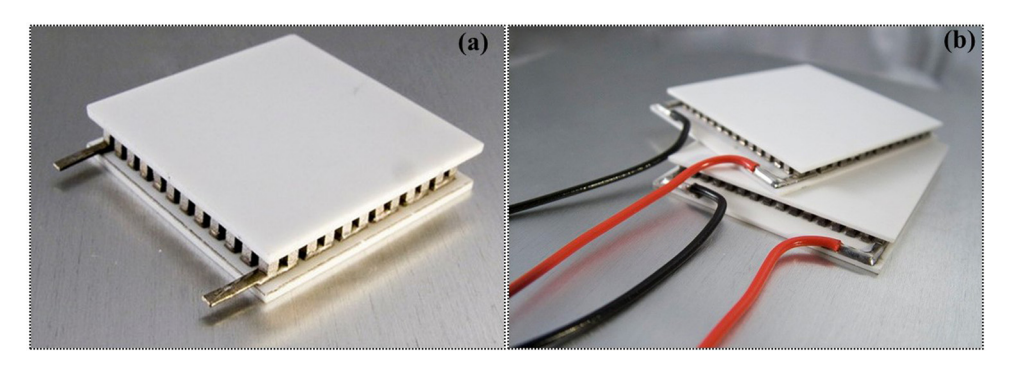


Figure 5: (a) Thermoelectric module and (b) thermoelectric generator.

6 — Syed Irfan et al. DE GRUYTER

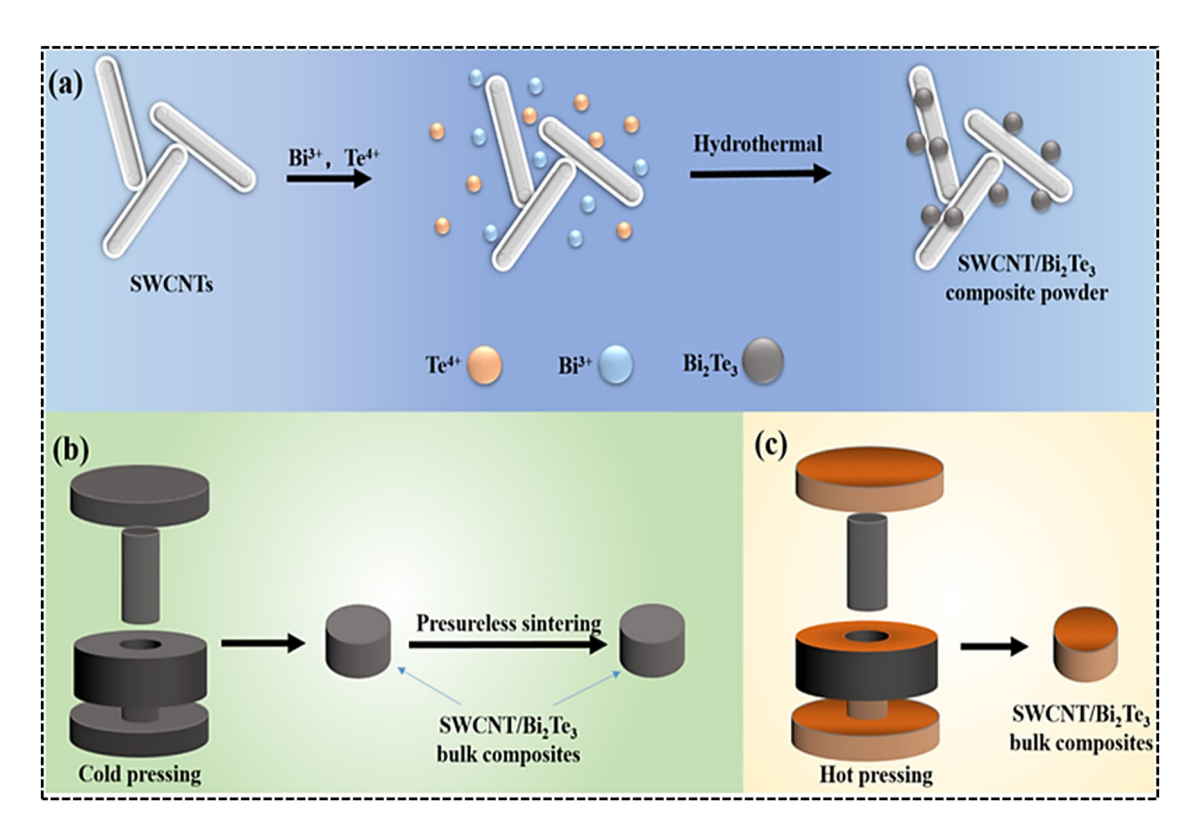


Figure 6: (a) Hydrothermal process, (b) Cold pressing and (c) Hot pressing, reproduced with the permission of Liu et al. [79].

3.1 Hydrothermal (HD) method

One of the most popular and efficient ways to create nanomaterials (Nan-Mat) with diverse morphologies is HD. This method uses an autoclave to conduct the reaction at high temperatures and pressures while using water or an organic substance as the reactants. The name "hydrothermal process" (HD) refers to the use of water throughout the preparation process [54,55]. Comprehensive discussions on various autoclave types and their purposes have also been reported in the literature [56,57]. Teflon-lined autoclaves can often withstand high temperatures and pressures [58]. Compared to glass and quartz autoclaves, it tolerates alkaline media and greatly resists hydrofluoric acid. A Teflon-lined autoclave is the best container to react under the necessary circumstances. The main element that makes it possible to synthesize different nanostructured inorganic materials during the HD process is precise control [59]. This technique can stimulate hydrolysis by crystal growth, resulting in the self-assembled Nan-Mat in solution. It can also facilitate and speed up the interaction between the reactants. In addition, it is simple to tune the characteristics, morphology, size, and structure of Nan-Mat by adjusting the various parameters, such as temperature, reactant concentration, reaction medium, pressure, pH, reactant concentration, reaction time, as well as the filled capacity of the autoclave. The following steps are part of the HD synthesis process: (i) preparing precursors by combining soluble metal salt using aqueous solution, (ii) combining the solution into an autoclave to start the reactions at an elevated temperature and pressure, and (iii) finalizing the process by filtering, washing, and then drying [60]. Many Nan-Mat have been studied using the HD technique [61–79].

3.2 Sol-gel method

Currently, numerous methods and techniques are employed to produce nano-materials. However, the sol–gel technique is mainly used for industrial purposes because of its more comprehensive range of applications [80–84]. The industrial-level employment of this technique is due to producing high-quality nanoparticles in large quantities [85–87]. It is also used for metal oxide nanoparticles and mixed oxide composites. The surface and textural characteristics of the materials might be manipulated using this technique. The sol–gel procedure primarily goes through three steps to get the final metal oxide treatments: drying [88], hydrolysis [89], and condensation [90]. The process of creating metal oxide comprises many sequential processes (Figure 6).

First, the matching metal precursor quickly hydrolyzes to generate a metal hydroxide solution, which is immediately condensed to form 3D gels. Depending on the drying method, the resultant gel can be transformed into Xerogel or Aerogel [91]. Depending on the solvent used, the sol-gel process may be divided into two categories: aqueous sol-gel and nonaqueous sol-gel [92]. The aqueous sol-gel technique uses water as the reaction medium, whereas the nonaqueous sol-gel technique uses organic solvents for reaction media. Figure 7 depicts the chemical route used in the sol-gel process to produce metal oxide nanostructures [93]. The metal precursor and solvent composition in the sol-gel process is essential for creating metal oxide Na-Par. In the agueous sol-gel method, water solvent provides the oxygen, which is required for the formation of metal oxide. Typically, the metal precursors used in this process include metal acetates and nitrates. However, due to the strong attraction of alkoxides to water, metal alkoxides are often utilized as precursors for forming metal-oxide nanoparticles [94,95]. The aqueous sol-gel approach does come with specific challenges, though. In various situations, the crucial steps - hydrolysis, condensation, and drying - occur concurrently, making it challenging to regulate particle shape and ensure reproducibility of the end procedure during the sol-gel method [96]. The nonaqueous sol-gel technique uses solvents such as ketones, aldehydes, alcohols, or metal precursors to provide the oxygen needed to create metal oxide.

These organic solvents also deliver oxygen while providing a flexible tool for adjusting several essential factors, including the final oxide material's composition, particle size, surface characteristics, and morphology. Although nonaqueous sol–gel approaches are less well known than aqueous sol–gel

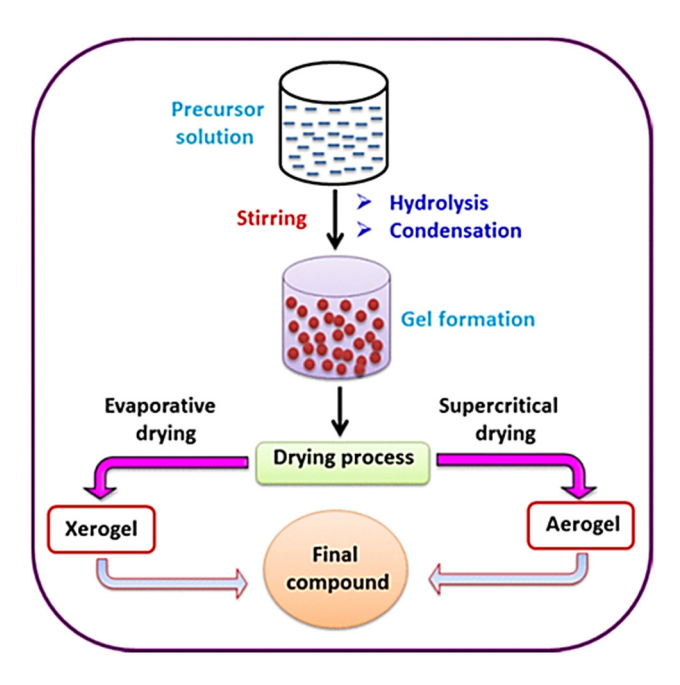


Figure 7: Sol–gel method, reproduced with the permission of Adschiri *et al.* [100].

approaches, they have demonstrated superior effects on synthesizing nano-oxides compared to aqueous sol–gel process. The generation of metal oxide nanoparticles, a non-aqueous sol–gel pathway, may be separated into two key strategies: surfactant-controlled and solvent-controlled approaches [93]. The hot injection approach uses a surfactant-controlled strategy that directly transforms metal precursor into metal oxide at higher temperatures. Some recent examples are as follows: Bi₂Te₃ is one of the most widely used materials for thermoelectric applications due to its high thermoelectric efficiency. Sol–gel methods can synthesize Bi₂Te₃ nanoparticles or thin films, which can then be assembled into TEMs.

Similarly, the PbTe is another commonly used thermoelectric material, especially in high-temperature applications. Sol–gel techniques can fabricate PbTe nanoparticles or thin films for constructing TEMs. Also, the SiGe alloys exhibit good thermoelectric properties, particularly at elevated temperatures. Sol–gel processes can deposit SiGe thin films or nanoparticles, which can be integrated into TEMs. Sam as copper selenide is an emerging thermoelectric material known for its nontoxicity and earth abundance. This method can synthesize Cu₂Se nanoparticles or thin films, which can be incorporated into TEMs. This technique eliminates particle agglomeration and allows for excellent control over the formation and development of the Na-Par [93].

3.3 Polyol method

Different types of Na-Par with various morphologies have been created using several potential synthetic techniques [97]. Among these, the polyol approach is a flexible liquidphase technique that uses multivalent alcohols and high boiling to create Na-Par [98]. Polyols can regulate the development of particles in addition to acting as a solvent and reducing agent. The Fievets group adopted the word polyol for synthesizing metal nanoparticles in 1989, which marked the beginning of the polyol synthetic pathway. This process has been used with various polyols, including diethylene, ethylene, propylene, triethylene, tetraethylene, butylene, and polyethylene glycol. Moreover, Carroll et al. synthesized elemental copper and nickel nanoparticles using the polyol method and investigated further with theoretical calculations [99]. However, polyols offer fantastic benefits in several ways. Several reports have been published using polyol methods, such as Grisaru et al. who reported the microwave-assisted polyol method was quite impressive for the fabrication of CuInTe₂ and CuInSe₂ nanoparticles. Also, simple and inexpensive metal precursors can be used as

starting compounds because of polyols' excellent beginning material solubilization properties [101,102]. Riyang *et al.* used the polyol reduction method to synthesize a highly dispersed Ru/SiO₂-ZrO₂ catalyst. The chelating characteristics of the polyol aid in controlling crucial elements of the particle nucleation, growth, and aggregation processes. Another important advantage of polyols is their ability to swiftly reduce metal solutions to produce metal Na-Par at higher temperatures [103]. When choosing a polyol to synthesize Na-Par, the boiling point and reduction potential must be considered.

3.4 Bridgman method

Single crystals may be grown under controlled conditions using the Bridgman method. The crystal formation of choice can be achieved using a regulated temperature gradient [104]. The gradient may be changed by adding various temperature regions to the system or by adjusting the system's overall temperature. This process can produce single crystals in semiconductors and other electrical devices [105,106].

The polycrystalline material is heated over its melting point in an oven using the Bridgman method. A vertical and a horizontal orientation may be used to develop the crystals. Their somewhat differing cooling systems are what distinguish the two approaches. Dynamic vertical single-

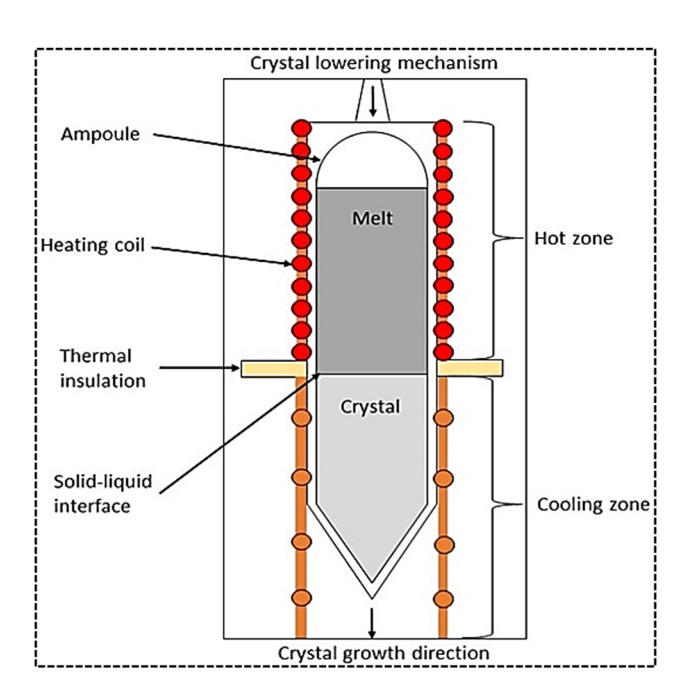


Figure 8: Illustration of the Bridgman method, reproduced with the permission of Mohamed *et al.* [117].

crystal development is shown in Figure 8. The approach has historically relied on a dynamic cooling mechanism, with hot and cold zones in the oven. In an ampoule, the melt (Figure 8) is swirled before being transferred through the cooling area of the oven. The nucleation takes place lengthwise in the cold end of the oven, and the single crystal formation begins at the end of the hot zone. To create a homogeneous crystal, cooling during crystallization should be gradual. The cooling rate is determined by the material and the product's requirements. When the crystal is completely formed, the system is cooled down to room temperature. The domain crystalline substance is afterward returned to the melt [105]. In a static cooling setup, the melt does not move as an ampoule's temperature varies over time. The procedure is carried out in a coil-equipped melting oven. Because the process requires constant regulation of the temperature gradient, the oven must support certain temperatures. Ovens can be of many sorts, some providing temperature control in a single or numerous zones. Most melting ovens are appropriate for controlling the temperature in one zone of static cooling systems. There must be several temperature zones in dynamic cooling systems. For instance, because tube ovens allow for numerous temperature zones, they are frequently employed in Bridgman techniques.

3.5 Czochralski method (CZ)

In the CZ process, a small crystal is first inserted into a melt-in crucible, which pulls the seed upward to produce a single crystal [106]. This method of creating nanoparticles approach was established in 1916 by Jan Czochralski. The technique produces numerous single crystals, including Si and Ge [107]. Several researchers have used the CZ approach to create single crystalline SiGe. Kürten et al. used a prolonged pulling rate during the CZ development of Si-rich SiGe to create a stable liquid-solid interface. In addition, the gas flow shape was designed to ensure superior temperature stability. As a result, single-crystalline SiGe was produced with a Ge concentration of up to 0.2 [108]. Yonenaga et al. have thoroughly investigated Si_{1-x}Ge_x CZ development across the whole range of Ge content and has produced single crystals for 0 < x < 0.1 and 0.85 < x < 1[109–114]. Poly-crystals were formed with an intermediate Ge concentration. On the basis of Tiller's criteria [115], they calculated the critical growth velocity of occurrence for constitutional super-cooling as a function of Ge concentration at a specific temperature gradient. However, poly-crystallization was seen for the intermediate Ge content even when the growth velocity was slower than the critical value [116].

No special attention was paid to the homogeneity of Ge content, and the Si depletion was seen in the pulling direction. Deitch et al. [118] proposed a modified CZ technique. They employed pre-grown large-diameter single-crystal Si seeds to speed up cap crystallization and guarantee a single crystal in a large crystal diameter. In actuality, SiGe single crystals with a Ge concentration of up to 0.17 and a diameter of 68 mm were produced. Abrosimov et al. employed Si rods for continuous Si feeding to the melt (Figure 9) to prevent Si depletion during the CZ development of SiGe [119]. They have tried to maintain a consistent Ge content in SiGe by regulating the Si rods' movement rate and the rate at which the developed crystal is pulled. Global modeling of the entire chain, including Si dissolution across the solid-liquid interface and the transport in the melt, will be required to optimize the process.

3.6 Conjugated polymers

However, inorganic semiconductor materials have a few intrinsic drawbacks, such as high manufacturing costs, toxicity, poor processability, and scarcity. Furthermore, most high-performance inorganic TE materials work best at temperatures above 200°, so they cannot satisfy the growing need to capture waste heat below 150° [120]. However, there may be answers to the issues with organic semiconductors, which have been disregarded in recent

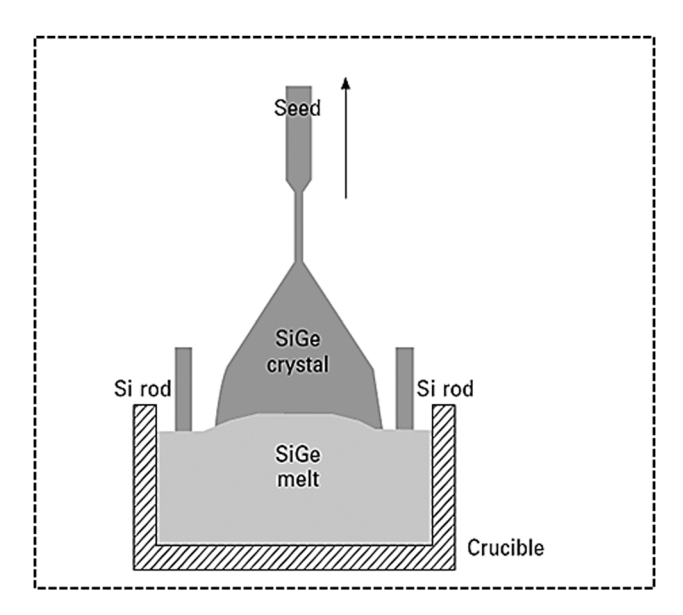


Figure 9: Diagram illustrating the CZ development of a bulk SiGe crystal with Si being continuously added to the melt, reproduced with the permission of Wei *et al.* [120].

decades because of their low energy conversion efficiency and potentially poor thermal stability. Conducting polymers, for example, are interesting candidates for organic semiconductors because they can convert low-end thermal energy into usable electricity [121]. This could lead to developing larger-area, more flexible, low-toxicity, and sustainable TEDs [122]. Over the past 10 years, significant efforts have been made to enhance the performance of organic thermoelectric materials. These efforts include the development of novel molecular design strategies and the creating of nanocomposites that combine nanomaterials and conducting polymers [123].

3.7 Graphene

Two-dimensional carbon lattice graphene has superior thermal and electrical characteristics [124]. Researchers' interest in studying the thermoelectric properties of graphene skyrocketed following its discovery as the best conductor of heat and electricity. While graphene's exceptional electrical conductivity can be attributed to its ultrahigh carrier mobility (15,000 cm²·V⁻¹·s⁻¹), its exceptionally high thermal conductivity (which can reach up to 2,500–5,000 W·m⁻¹·K⁻¹) poses a significant obstacle to its application as a thermoelectric element [125] Furthermore, generating an effective thermoelectric voltage in graphene is challenging due to its low Seebeck coefficient, commonly 10–100 μV·K⁻¹ [126]. Except for a few recent investigations, all these variables contribute to the extremely low reported ZT values for pristine graphene, which are approximately 10⁻⁴. For instance, a record-high ZT of 0.1 has been recorded in suspended graphene nanoribbons with widths of about 40 nm and lengths of about 0.25 microns. In contrast, a typical semiconductor has a respectable ZT of 1-2 [127].

4 Uniqueness of bismuth telluride

In recent years, TEMs have been extensively explored in terms of their characteristics, structure, and TE capabilities with various dopants. Many of these dopants give information about their features. This section examines the dopants utilized in the current and past and their influence on the TE characteristics of novel alloys. Bi_2Te_3 and its companion substances were traditional TEM. Numerous TE cold modules with BiTe components have been extensively used in X-ray and laser detectors. According to theoretical calculations, the $5\,\text{Å}$ wide Bi_2Te_3 quantum wire might achieve the

maximum ZT value of 14 [128]. ZT might potentially rise by a factor of 13 when $\rm Bi_2Te_3$ is used in a quantum-well arrangement [129]. Density functional simulations were used to examine the TE characteristics of $\rm Bi_2Te_3$ nanowires. The ZT value for nanowires with a width of N=5 and a [130] growth direction was 2.3 at 300 K and 2.5 at 350 K [131]. BiTe TEM characteristics varied depending on the preparation techniques used. The more energy used for material fabrication, the greater the efficiency of TE.

From liquid to solid, from low temperature to high temperature, and from straightforward to complex methods, these can affect the production of nanoparticles, and the ZT was affected by these methods [132]. The HD process was used to synthesize nano-powders of Bi_2Te_3 , $R_{0.2}Bi_{1.8}Te_3$ (whereas R =Sm, Y, Ce) [133] and $Bi_2Te_{3-a}I_a$ (a = 0.0, 0.05, 0.1, 0.2) [134]. The samples of $Bi_2Te_{2.85}Se_{0.15}: X_a$ (X = I, C, Ag, Ni, and Zn) [135], $Bi_2(Te_{0.9}Se_{0.1})_3$ [136], and $Ag_xBi_2Te_{2.7}Se_{0.3}$ [137] were prepared using melting and hot pressing in encapsulation. Ajay et al. prepares Bi₂Te_{3-x}Se_x samples using the Polyol method [138,139]. Yang prepared N-type Bi₂Te₃:Pb doped with Pb using radio frequency magnetron sputtering, and Bi₂Te₃ films doped with Pb on SiO₂ substrates at room temperature. Smallsize Pb plates were used as the source materials, and silver paste was used to fix Pb plates to the Bi₂Te₃ target so that the doping concentration in the films could be changed [139]. The HD approach was used successfully to produce flowerlike nano-powder of $Tl_xBi_{2-x}Te_{3-x}I_x$. Then, heat and pressing are used to form bulks from the created nanoparticles [140]. Wu et al. prepared Bi_{2-x}Zn_xTe₃ single crystals using a modified Bridgman method to study its TE properties [141]. Singh et al. prepared Bi_{2-x}Gd_xTe₃ samples using the sol-gel method [142]. A KrF excimer laser was used to prepare Bi₂Te_{2.7}Se_{0.3} thin films with a high c-axis texture on fused silicon substrates. A commercially available Bi₂Te_{2.7}Se_{0.3} target was slightly enclosed with a platinum sheet (0.1 mm) along the diameter to form a thin nano-composite coating with platinum inclusions [143]. Hsin prepare polycrystalline $Bi_{40-\nu}Ge_xTe_{60-x+\nu}$ alloys using the Bridgman technique for the TE characteristics assessments [144]. CZ technique was used to create single crystals of Bi₂Te₃. Polycrystalline samples with grapheme (GR) doping were created using a solid-state reaction. The crystals were created using Bi and Te powders. Powders of Bi₂Te₃ were combined with GR, which was then crushed into prill and sintered at 520°C for approximately 600 min in argon [145].

 Bi_2Te_3 beads were used to create the Bi_2Te_3 powder and was then processed using zirconia balls in an inert environment to prevent oxidizing the particles' surfaces. A diluted HCl solution was used to rinse the ball-milled powder to remove any oxidized coatings on the surface. Based on the methods previously reported [146], with a few changes, the Bi_2Te_3 nano-wires were synthesized. A modified version of Hummers' approach, as described in earlier

published publications [147], was used to create GR oxidized nano-sheets. The produced GO sheets had several micrometers dimensions and a 4-5 nm thickness. The combination was first ultrasonicated for 1h after being suspended in 500 mL of deionized water containing GR oxidized and Bi₂Te₃ powder. After that, a suitable amount of N₂H₂-H₂O was added to limit the dispersion. This combination was cooked at 368 K for 2 h while being stirred. The finished item was filtered, cleaned with deionized water, and dried for 24 h at 333 K. To create the GR/Bi₂Te₃ -powder composites, the finished product was ground into an adequate powder, put into an iron mold, and hard-pressed under high pressure [148]. The composite specimen of Bi₂Te₃:G was made by incorporating 0.05% by weight of G into the Bi₂Te₃ powder [149]. These powders were well combined with agate mortar and pestle before being compressed into pellets. The pressure was applied to roomtemperature air to compact the powder. The samples were held in storage for 5-7 min. Similarly Bi₂Te₃:C composite sample was created by combining Bi₂Te₃ sample and graphite powder [150]. Qijiang et al.'s [108] study shows no notable impure phases such as tellurium, bismuth, or cerium are observed. The lattice parameters R_{0.2}Bi_{1.8}Te₃ are all significantly more significant than the Bi₂Te₃. The minor shift in the crystal characteristic can be due to the small changes in the radius of the atoms. SEM revealed that their morphologies change greatly when nano-powders are doped with rare earth elements. A specimen free of rare earth elements displays a flower-like appearance. Nano-sheets contract when Ce, Y, and Sm are introduced. It suggests that the doping of rare earth elements has a substantial impact on the shape of the powders. It is unknown why rare earth element doping may drastically alter morphology [151]. The presence of rare earth metals alters the bonds' robustness and significantly affects their growth [108].

Doping with rare earth elements boosts electron concentrations and lowers electrical resistance. The electrical resistivity of $R_{0.2}Bi_{1.8}Te_3$ is, nevertheless, more significant than that of un-doped Bi_2Te_3 [152]. There is an inverse relation between electrical resistivity and carrier mobility and concentration; hence, differences in carrier numbers will affect variations in electrical resistivity. Decreased carrier mobility will result in greater electrical resistivity – two plausible explanations for reduced carrier mobility of doped samples. First, substituting rare-earth elements can decrease the carrier mobility by amplifying alloy scattering. Second, chemical bonding can have a significant impact on carrier movement. Covalent bonds are generally more favorable for carrier movement than ionic components [153]. The fraction of the ionic part of the bond of two

elements may be determined using the conventional Pauling empirical equation and electronegativity of bonding atoms [154]. Temperature affects the Sb coefficients. The specimens display n-type conduction because of negative Sb coefficients in the investigated temperature [155]. The intrinsic excitation temperatures of $R_{0.2}Bi_{1.8}Te_3$ was 480 K, indicating similar intrinsic excitation temperatures (approximately 500 K) and band gap to binary Bi_2Te_3 . The thermal conductivity was decreased by substituting Ce, Sm, and Y [156]. The most effective dopant was Ce onto Bi_2Te_3 for reducing thermal conductivity. As a result, the ZT value of $Ce_{0.2}Bi_{1.8}Te_3$ reached to 1.29 at 398 K, higher than Bi_2Te_3 -based alloys but greater than zonemelting ingots [157–160] (Figure 10 and Table 1).

Wu et al. [134] explored I-doped Bi₂Te_{3-x}I_x nano-powders. The elemental diffraction scattering (EDS) investigation was done by gathering spectra from over 15 nano-crystals. The EDS and X-ray diffraction (XRD) measurements reveal that I was successfully doped onto Bi₂Te₃. The lattice characteristics of Bi₂Te_{3-x}I_x compounds derived by Rietveld refinement were all shorter than the Bi₂Te₃ lattice values (JCPDS15-0863 card). This is mostly due to I's smaller atomic radius (0.133 nm) compared to Te's (0.137 nm) [161]. The Nan-Mat showed flower-like morphology (x < 0.1) [162–165] and exhibits thick layers that are less than 100 nm in thickness. These morphologies were destroyed when the concentration of I was increased. The sheets of such morphologies became significantly smaller, so I doping does not prompt large nano-sheets. As the temperature climbed, the electrical resistivity of each sample increased, behaving as a degenerate semiconductor. The I-doped nanoparticle specimens from Bi₂Te_{2.9}I_{0.1} displayed electrical resistivity that was smaller than that of un-doped Bi₂Te₃ sample but

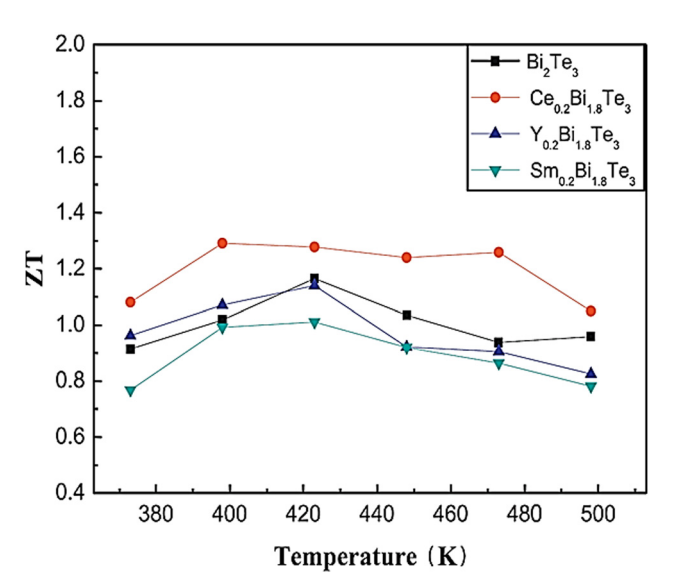


Figure 10: The ZT of $R_{0.2}Bi_{1.8}Te_3$ bulk samples \emph{versus} reproduced with the permission of [153].

Table 1: Lattice parameters of the prepared powders [138]

Sample	Bi ₂ Te ₃	$Ce_{0.2}Bi_{1.8}Te_3$	$Y_{0.2}Bi_{1.8}Te_3$	Sm _{0.2} Bi _{1.8} Te ₃
a(Å)	4.382	4.387	4.382	4.386
c(Å)	30.485	30.495	30.492	30.496

higher than those of ${\rm Bi_2Te_{2.95}I_{0.05}}$ and ${\rm Bi_2Te_{2.8}I_{0.2}}$ samples. It implies that the optimal level of I-doping is 0.1. Indicating that the specimens show n-type conduction, all samples had -ive Sb coefficients throughout the observed temperature range. A donor dopant is something like I replacing Te. After a maximum value was reached, continued temperature rise caused a reduction in Sb coefficients.

When n and p kinds of carriers are present, the bipolar effect may occur [166]. The specimen's power factor values are smaller than the un-doped sample's. This is the result of the Sb coefficient and electrical resistivity working together. Idoping reduces the Sb coefficient while increasing electrical resistance. However, in contrast to an un-doped sample, the power factor of the Bi₂Te_{2.9}I_{0.1} the sample is almost unaltered. The thermal conductivity variance between I-doped and undoped samples is nearly identical. Only the Bi₂Te_{2.9}I_{0.1} sample's value is marginally less than the amount of the un-doped sample. The Wiedemann-Franz equation for near-degenerate or degenerate semiconductors was used to calculate the electronic impact on thermal conductivity [167]. The lattice thermal conductivity has not changed much except for the value of the doped samples (x = 0.1) before 498 K. Three potential causes exist for the I-doping samples' continued reduced thermal conductivity. First, just like the un-doped Bi₂Te₃, the doped nanopowders have a flower-like shape. As a result, some minor grains are amid the bigger ones in the doped bulk, which is ideal for lowering thermal conductivity. Second, the I-doping would not significantly raise the phonon frequency since the respective atomic masses of I (126.9 g) and Te (127.6 g) are so near. Third, changing Te to I will result in additional alloying, which might surge phonon scatting, reducing thermal conductivity. The Bi₂Te_{2.9}I_{0.1} sample, which has a more excellent ZT value over the observed temperature span, can be attributed to a reduction in thermal conductivity and electrical resistivity. In contrast to commercial zone melting ingots, the ZT value of Bi₂Te_{2.9}I_{0.1} sample reaches a value of 1.1 at 448 K [168]. The ZT value of Bi₂Te_{2.9}I_{0.1} is also relatively high for an n-type TE material, especially considering that n-type alloys based on Bi₂Te₃ have recently seen significant improvements in ZT values above 1 [169,170] (Figure 11 and Table 2).

Wu *et al.* [135] investigated ways to increase TE performance by manipulating the carrier concentration by doping. This work used encapsulated melting and hot pressing to create solid solutions of $Bi_2Te_{2.85}Se_{0.15}$:D = I, Ni, Ag, Zn, and

12 — Syed Irfan et al. DE GRUYTER

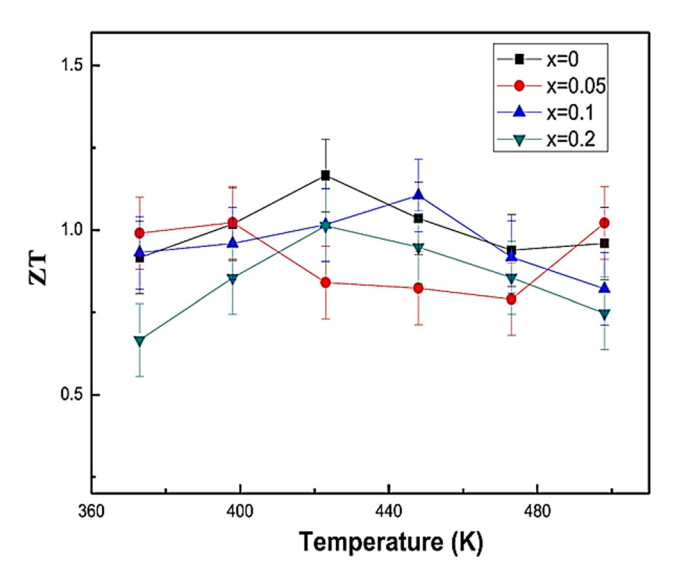


Figure 11: The ZT of $\mathbf{Bi_2Te_{3-x}I_x}$ bulk samples *versus* temperature, reproduced with the permission of Wu *et al.* [134].

Cu. Table 3 lists the electrical transport characteristics and the greatest figure of merit of $\mathrm{Bi_2Te_{2.85}Se_{0.15}}$:Dopants. Halogen element (I, occupies the Te site), which generates electrons, can increase the carrier concentration and decrease mobility. Though the transition elements and other dopants have taken up residence at the Bi site, the reduction in carrier concentration was observed, and mobility was enhanced. The phases and TE characteristics of the samples with the highest ZT for each doping element are listed below.

Table 2: Lattice parameters of as-synthesized powders [2]

Sample	Bi ₂ Te ₃	${\bf Bi_2Te_{2.95}I_{0.05}}$	$Bi_2Te_{2.9}I_{0.1}$	$Bi_2Te_{2.8}I_{0.2}$
a(Å)	4.381	4.377	4.373	4.370
c(A)	30.481	30.435	30.406	30.364

Hot-pressed Bi₂Te_{2.85}Se_{0.15}:Dopant XRD patterns were consistent with the literature, and a secondary phase was not discernible. Successful preparation of solid Bi₂Te_{2.85}Se_{0.15}:Dopant solutions with excellent crystallinity was achieved. The compositions and lattice constants for a few samples are listed in Table 3. The dopant's quantity was too small; hence, it did not impact diffraction patterns and the constant value of the lattice. The assynthesized samples were electrical conductivities marginally reduced as the temperature rose, indicating degenerate semiconductor behavior. By acting as an electron donor, I doping boosted electrical conductivity. However, the electrical conductivities of the other dopants were similar to or lower than those of Bi₂Te_{2.85}Se_{0.15}, acting as electron acceptors. Samples showed negative Sb coefficients at each of the temperatures used to test them, which is consistent with the Hall coefficients' negative sign and indicates n-type semiconductor properties. The reduction in carrier concentration enhanced absolute values of the Sb coefficient for copper and Argon doping Bi₂Te_{2.85}Se_{0.15} while not affect I-, Ni-, and Zn-doped Bi₂Te_{2.85}Se_{0.15} (Table 4).

When I resides at the Te-site, the electron is produced, increasing the carrier concentration and, thus, the electrical conductivity [171]. This led to an improvement in

Table 3: Electrical transport characteristics and figure of merit of Bi₂Te_{2.85}Se_{0.15}:Dopant [135]

Samples	Hall coefficient (cm³⋅C ⁻¹)	Mobility (cm ² ·V ⁻¹ ·s ⁻¹)	Carrier Conc. (cm ⁻³)	ZT _{max}
Bi ₂ Te _{2.85} Se _{0.15}	-0.085	92.58	7.37 × 10 ¹⁹	0.57@99.85°C
$Bi_2Te_{2.85}Se_{0.15}:I_{0.0025}$	-0.076	85.67	9.38 × 10 ¹⁹	0.76@99.85°C
Bi ₂ Te _{2.85} Se _{0.15} :I _{0.005}	-0.058	92.93	1.07×10^{20}	0.90@149.85°C
Bi ₂ Te _{2.85} Se _{0.15} :I _{0.01}	-0.046	81.84	1.36 × 10 ²⁰	0.77@199.85°C
Bi ₂ Te _{2.85} Se _{0.15} :I _{0.015}	-0.029	62.21	2.14 × 10 ²⁰	0.71@199.85°C
Bi ₂ Te _{2.85} Se _{0.15} :I _{0.03}	-0.017	42.65	3.63 × 10 ²⁰	0.60@259.85°C
Bi ₂ Te _{2.85} Se _{0.15} :I _{0.045}	-0.015	48.60	4.22×10^{20}	0.47@249.85°C
Bi ₂ Te _{2.85} Se _{0.15} :Cu _{0.045}	-0.135	123.94	4.62 × 10 ¹⁹	0.58@149.85°C
Bi ₂ Te _{2.85} Se _{0.15} :Cu _{0.0075}	-0.131	120.60	4.78 × 10 ¹⁹	0.64@99.85°C
Bi ₂ Te _{2.85} Se _{0.15} :Cu _{0.01}	-0.175	144.48	3.56 × 10 ¹⁹	0.76@49.85°C
Bi ₂ Te _{2.85} Se _{0.15} :Cu _{0.015}	-0.190	135.18	3.28 × 10 ¹⁹	0.71@49.85°C
Bi ₂ Te _{2.85} Se _{0.15} :Ag _{0.005}	-0.176	142.44	3.54 × 10 ¹⁹	0.65@99.85°C
Bi ₂ Te _{2.85} Se _{0.15} :Ag _{0.01}	-0.171	143.59	3.65 × 10 ¹⁹	0.75@99.85°C
Bi ₂ Te _{2.85} Se _{0.15} :Ag _{0.015}	-0.213	123.44	2.93 × 10 ¹⁹	0.68@49.85°C
Bi ₂ Te _{2.85} Se _{0.15} :Ag _{0.02}	-0.245	136.12	2.54 × 10 ¹⁹	0.68@49.85°C
Bi ₂ Te _{2.85} Se _{0.15} :Ag _{0.03}	-0.320	102.97	1.95 × 10 ¹⁹	0.40@49.85°C
Bi ₂ Te _{2.85} Se _{0.15} :Ni _{0.005}	-0.083	90.68	7.56 × 10 ¹⁹	0.56@99.85°C
Bi ₂ Te _{2.85} Se _{0.15} :Ni _{0.01}	-0.279	118.41	2.23×10^{19}	0.32@49.85°C
Bi ₂ Te _{2.85} Se _{0.15} :Zn _{0.005}	-0.084	98.37	7.39×10^{19}	0.57@99.85°C
$Bi_2Te_{2.85}Se_{0.15}:Zn_{0.01}$	-0.176	113.25	3.56×10^{19}	0.51@49.85°C

Table 4: Lattice parameters of the prepared powders [135]

Sample	a(Å)	c(Å)
Bi ₂ Te _{2.85} Se _{0.15}	4.438	3.042
$Bi_2Te_{2.85}Se_{0.15}$: $I_{0.005}$	4.437	3.048
Bi ₂ Te _{2.85} Se _{0.15} :Cu _{0.01}	4.437	3.040
$Bi_2Te_{2.85}Se_{0.15}:Ag_{0.01}$	4.437	3.040
Bi ₂ Te _{2.85} Se _{0.15} :Ni _{0.005}	4.438	3.035
$Bi_{2}Te_{2.85}Se_{0.15}$: $Zn_{0.005}$	4.437	3.039

the PF value for the I-doped solution. In contrast, a hole is created when Cu and Ag atoms replace the Bi site, which lowers carrier concentration [172,173]. The Cu doping prevents the development of BiSe antisite flaws, which prevents the free electron concentration from rising. The enhanced power factor from I, Cu, and Ag doping improved the ZT value, having ZT value 0.90 at 423 K for $Bi_2Te_{2.85}Se_{0.15}$: $Cu_{0.005}$ peak and 0.76 at approximately 49.85°C for $Bi_2Te_{2.85}Se_{0.15}$: $Cu_{0.01}$ was obtained. The improved carrier concentration should increase the ZT value according to the operating temperature (Figure 12).

To improve TE ambient temperature efficiency of n-type polycrystalline, $\mathrm{Bi_2Te_{2.85}Se_{0.15}}$ alloys were investigated by Lee *et al.* [137], who reported an integrated optimization approach of Ag doping with hot compression. Bismuth-tell-uride-based alloys have long been the finest commercial TEM for solid-state refrigeration near ambient temperature. Both traditional zone-melted p- and n-type $\mathrm{Bi_2Te_3}$ -based alloys display ZT \sim 1 near the 22°C ambient temperature. However, because of their weak mechanical qualities, the

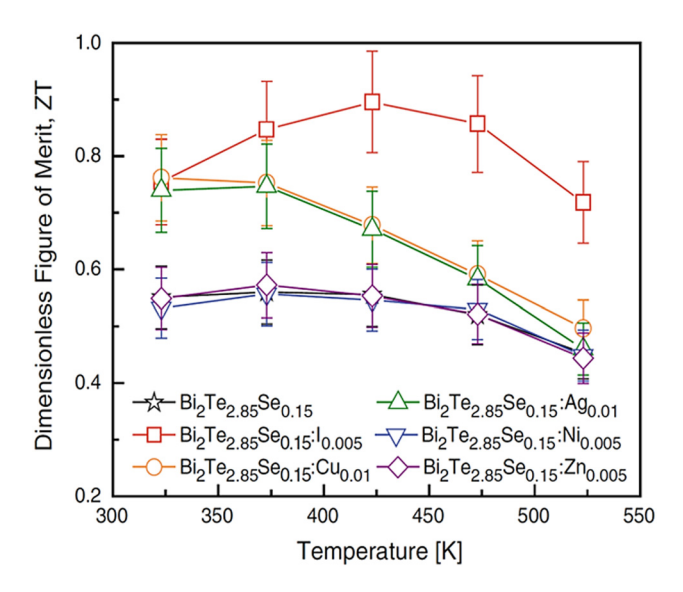


Figure 12: Figure of merit temperature dependency, reproduced with the permission of Wu *et al.* [135].

construction of devices often fails. In comparison to zonemelted equivalents, which have received a lot of focus recently, polycrystalline Bi₂Te₃-based alloys prepared by metallurgical processing methods offer better mechanical properties and a lower lattice contribution. To attain a high peak ZT > 1.2 and room temperature ZT > 1.0 in p-type (Bi, Sb)₂Te₃ alloys, nano-structuring methodologies, including the "bottom-up" approach [174-180] and the "top-down" approach [181-183], have been utilized. The lowered ZT may be due to significantly reduced carrier mobility mH following nano-structuring in n-type Bi₂(Te, Se)₃ alloys. Recent years have seen the effective application of the heat deformation (HD) method, which has been widely used in metallic alloys [184,185], to increase the mH of polycrystalline n-type Bi₂Te₃-based alloys. By repressing the Bi₂Te_{2.7}Se_{0.3} alloy, Hou et al. [186] found enhancement in the peak of ZT from 0.85 to 1.04 at 400K. Yan et al. got a ZT 1.06 at 400 K in the repressed Cu_{0.01}Bi₂Te_{2.7}Se_{0.3} sample [187]. Lee et al. [137] studied typically Ag_xBi₂Te_{2.7}Se_{0.3} samples. After heated deformation, it is clear that the (00l) diffraction intensity rises in the HD samples, showing a favored alignment. The orientation factor F of the (001) plane is determined using the Lotgering technique [188] to explore the texture degree further. By combining Ag doping and heat distortion, the service temperature of n-type polycrystalline Bi₂Te₃-based alloys is lowered from around 177–22°C. The power factor increases, but the electrical thermal conductivity close to 22°C decreases due to Ag doping's optimized carrier concentration. Due to shaping, the hot deformation procedure makes the carrier more mobile. The doubly hot, deformed Ag_{0.011}Bi₂Te_{2.7}Se_{0.3}, an alloy ore exhibits a ZT value of approximately 1.0 at 26.85°C and, and a peak ZT value of 1.1 at 76.85°C, which is encouraging for actual usage in refrigeration near ambient temperature (Figure 13).

Wu *et al.* [138] studied how $Bi_2Te_{3-x}Se_x$ nano-platelet composites made using the polyol technique have improved TE properties. Although the computed lattice parameters nearly adhere to Vegard's rule, two-mode behavior for $Bi_2Te_{3-x}Se_x$ nano-platelet are demonstrated by a break in shifting the high-frequency phonon modes. SPS pellet composites exhibit semiconducting behavior for intermediate Se compositions and metallic conduction for Bi_2Te_3 nano-platelet composites in terms of electrical resistivity. In all fabricated nano-platelet composites, the thermal conductivity is substantially lower than the bulk numbers and is mainly caused by scattering from microstructural grain boundaries. In compared to Bi_2Te_3 nano-platelet composites, the TE power of S (259 V·K⁻¹) and ZT is 0.54, approximately four times higher for $Bi_2Te_{2.7}Se_{0.3}$ SPS pellets (Figure 14).

Tentatively, this improvement in TE properties in nano-platelet composites is accredited to extensive grain 14 — Syed Irfan et al. DE GRUYTER

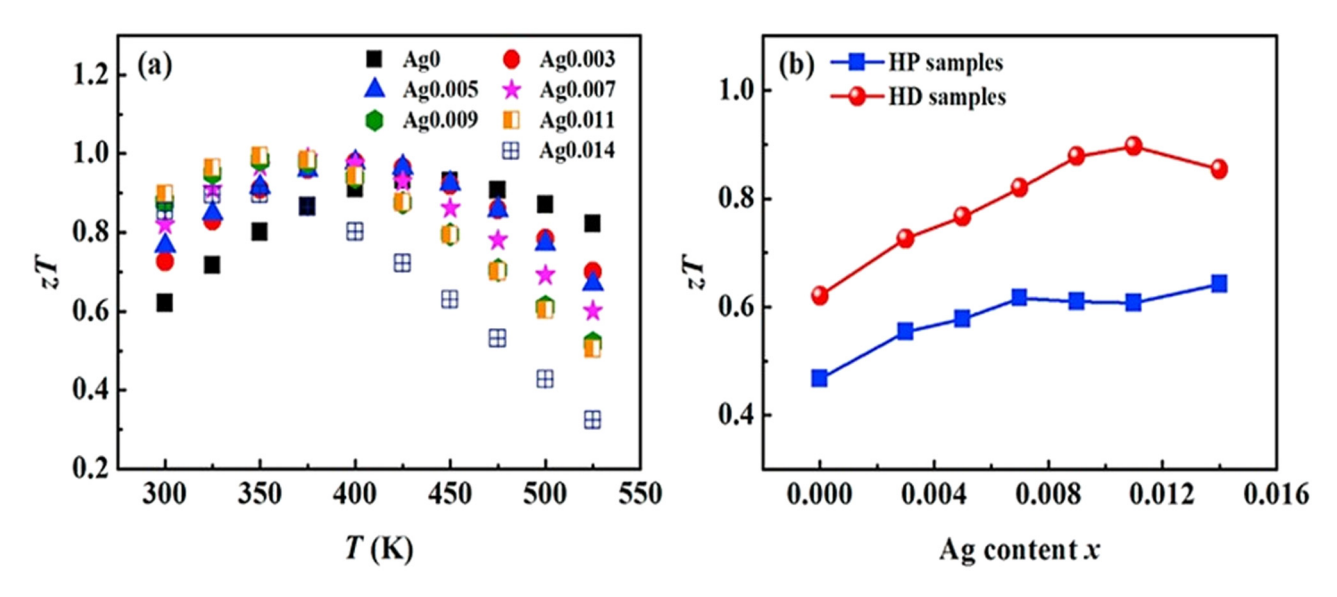


Figure 13: (a) The figures of merit (ZT) of $Ag_xBi_2Te_{2.7}Se_{0.3}$ samples *versus* temperature. (b) ZT *versus* Ag content, reproduced with the permission of [137].

boundaries in aligned nano-composites that filter low-energy electrons. In a study by Soni *et al.* [139], Pb-doped nano-crystalline n-type Bi₂Te₃ thin films were deposited by radiofrequency magnetron sputtering. The element Pb is suitable for adjusting the carrier concentration of bulk Bi₂Te₃ and doping Pb atoms into the crystal lattice of the material increases the concentration of holes [189,190]. Because typical n-type Bi₂Te₃ films have a high carrier concentration, ZT enhancement is constrained [191–194]. Pb doping reduced the carrier concentration of n-type Bi₂Te₃ films and increase TE characteristics of the Bi₂Te₃ film.

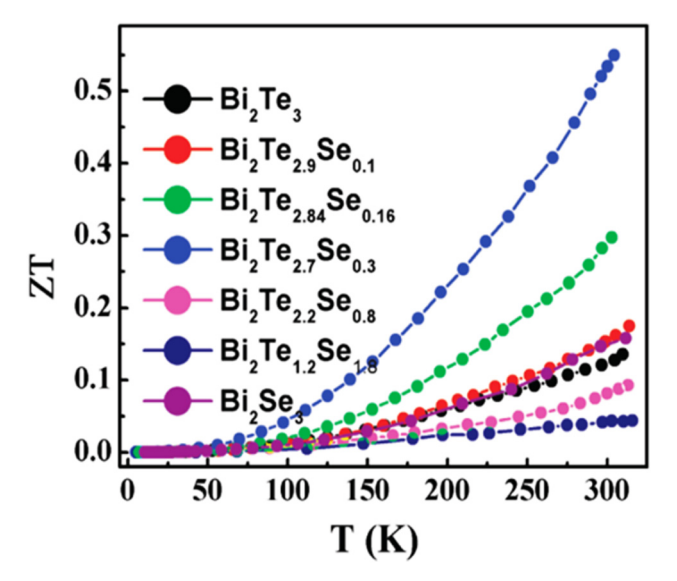


Figure 14: The ZT of ${\bf Bi_2Te_{3-x}Se_x}$ samples with temperature, reproduced with the permission of Wu *et al.* [138].

Pb doping allows for precise control of the Bi₂Te₃ films' carrier levels, which have a compelling effect on the transport properties of thin film. The Sb coefficient of Bi₂Te₃ films are highest, and thermal conductivity was lowest at Pb doping concentration. The PF values of 2.50 and 2.15 mW·K⁻²·m⁻¹ were achieved at 200°C, approximately for unannealed and annealed films doped with 0.38% Pb, respectively. The results showed that Pb doping was a workable method for improving the TE characteristics of n-type Bi₂Te₃ films. A potential material for TE micro devices is the Pb-doped Bi₂Te₃ sheet [140]. The HD process was successfully used by Wu et al. [141] to create Tl_xBi_{2-x}Te_{3-x}I_x nano-powders that were similar to flowers. After that, heat pressing was used to compress the created nanoparticles into bulks. The bulk samples of $Tl_xBi_{2-x}Te_{3-x}I_x$ were examined, and their TE characteristics were reviewed. The outcomes show that the effects of Tl doping were greater than those of I doping onto Bi₂Te₃ on electrical resistivity and Sb coefficients of Bi₂Te₃. The co-doped bulks' PF was consequently lower than the bulk Bi_2Te_3 . The $Tl_xBi_{2-x}Te_{3-x}I_x$ bulk samples' thermal conductivities continue to be lower. The results showed that at 398 K, the ZT value of the doped bulk $Tl_{0.1}Bi_{1.9}Te_{2.9}I_{0.1}$ reaches the value of 1.1 [140] (Figure 15).

New groups of surface materials that have time reversal protection by time-reversal symmetry are named topological insulators [195]. Consequently, the delocalized surface state is unchanged by nonmagnetic dopants and defects. The unusual features of TIs, such as the anomalous quantum Hall effect [195–203], hold great promise for the development of quantum computing. It was demonstrated using ARPS in $\mathrm{Bi}_2\mathrm{Te}_3$ and $\mathrm{Bi}_2\mathrm{Te}_3\mathrm{Tl}_s$ that quantum magneto-transport phenomena, like weak anti-localization [204–206], Aharonov-Bohm oscillations [207], and quantum conductance fluctuations

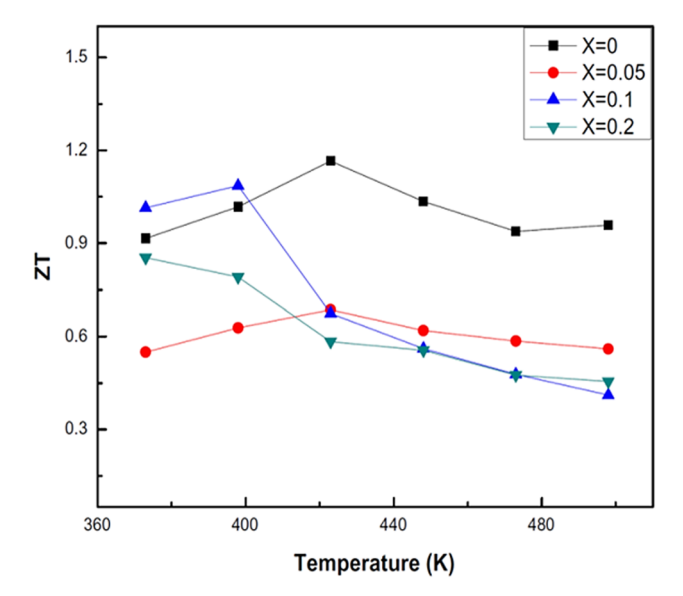


Figure 15: The ZT of $TI_xBi_{2x}Te_{3-x}I_x$ samples *versus* temperature, reproduced with the permission of Zhou *et al.* [140].

[208], are associated with topological surface states. Furthermore, strong TE properties in these materials are crucial because TE devices are considered a viable source of power generation and energy conservation. In these devices, n- and p-type materials are coupled in series. Bi_{2-x}Zn_xTe₃ single crystals that were created utilizing the modified Bridgman technique were investigated by Singh et al. [142]. He studied Zn-doped Bi₂Te₃ topological insulator's electrical resistivity, TE power, magneto-transport, and magnetism. Higher Zn content improves electrical conductivity, and calculated carrier mobility from Hall effect approaches, a phenomenal value of 7.2×10^3 cm²·V⁻¹·s⁻¹. In high-mobility specimens, a significant positive magnetoresistance was seen. It is notably shown that higher Zn-doped Bi₂Te₃ samples break the link between electrical conductivity and the Sb coefficient, significantly improving the TE power factor. Singh et al. [142] investigated the synthesis of bismuth telluride doped with the rare earth element gadolinium in two distinct configurations, 0.0 and 0.1. XRD was employed for structural investigation, which covered crystal structure, phase purity, crystallite size, and lattice characteristics. The rhombohedral structure of Bi₂Te₃ was revealed by the structural investigation. N-type Bi₂Te_{2.7}Se_{0.3} thin films containing Pt nano-inclusions were effectively made using pulsed laser deposition, according to Arif et al. and Sun et al. [143,144].

The grain borders of these semiconductor matrices include embedded Pt nano-inclusions. The PF of a nano-composite thin film may be significantly increased by adding Pt nano-inclusions thanks to the energy-filtering outcome. At the same time, the thermal conductivity was decreased *via* scattering long-wavelength phonons. The PF

reaches 3.5×10^{-3} W·m⁻¹·K⁻² at approximately 22°C with a ZT value of 1.17 thanks to the Pt content optimization. This preparation technique helps the production of anisotropic materials for TE and other renewable energy solutions, as well as the nano-engineering of textures and semiconductors. By gathering information on phase equilibrium from various thermally equilibrated ternary alloys and the three constituent binary systems, Wu et al. [145] studied the 523 K isothermal section of the Bi-Ge-Te system (Figure 16). In particular, the ternary system emphasizes the compositional homogeneity, phase relations, and thermal stability within the range restricted by BiTe, GeTe, and Te phases. At 523 K, the thermal stability of four ternary compounds, Bi₂Ge₃Te₆, Bi_{1.5}Ge_{1.5}Te₅, Bi₂Ge₁Te₄, and Bi₄Ge₁Te₇, is about along the Bi₂Te₃ - GeTe. When the nominal compositions fulfill specific requirements, $Bi_{40-\nu}Ge_xTe_{60-x+\nu}$ alloys $(x = 0 \rightarrow 12.5, y = 0 \rightarrow 10)$ were formed by Bridgman technique, and massive carrier transits from p-type holes for an un-doped stoichiometric sample to n-type electrons. Te must be less than 60.0 or 60.0 at.% and Ge/Bi greater than or equal to 0.2.

Among the alloy p-type (P2), the peak value of ZT is at 0.9 at 325 K, and in the case of n-type (N5), the alloy peak value of ZT is at 0.45 at 525 K, which traces in a Bi_2Te_3 + $Bi_2Ge_1Te_4$ + $Bi_4Ge_1Te_7$ three-phase region (Figures 17 and 18).

The recently established one-atom thick graphite, graphene (GR) [209], is crucial for understanding physics and real-world applications. Due to its extremely high mobility, it showed high electrical conductivity at approximately 22°C. A small amount of GR inserted into the **Bi**₂**Te**₃ matrix may be able to play a significant role in inhibiting phonon

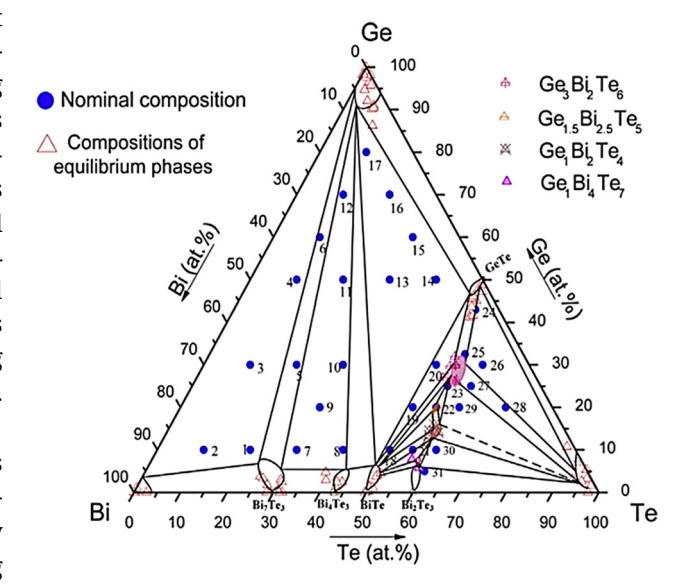


Figure 16: Ternary **Bi–Ge–Te** system, reproduced with the permission of Wu *et al.* [145].

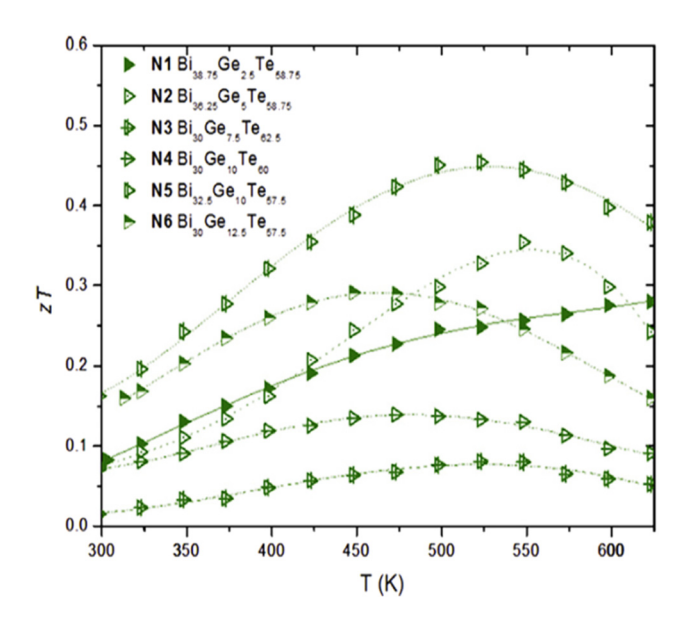


Figure 17: The ZT of $\mathbf{Bi}_{40-y}\mathbf{Ge_x}\mathbf{Te}_{60+x+y}$ with temperature, reproduced with the permission of Wu *et al.* [145].

transport while retaining the excellent electrical conductivity of the ${\bf Bi_2Te_3}$ lattice. In this research, both single crystals of ${\bf Bi_2Te_3}$ and ${\bf Bi_2Te_3}$ doped with GR have had their electrical structure and TE characteristics examined. Wu *et al.* [145] used CZ technique to create single crystals of ${\bf Bi_2Te_3}$. ${\bf Bi_2Te_3}$ polycrystalline samples with GR doping were created utilizing a solid-state reaction. The crystals were made using Bi and Te powders. The thermal power is approximately $190 \, {\rm V K^{-1}}$, same as for ${\bf Bi_2Te_3}$ [210]; resistivity was approximately $2.2 \, {\rm m}$ cm and reduces monotonically with declining

temperature for the $\mathbf{Bi_2Te_3}$ crystals. The thermal conductivity of $\mathbf{Bi_2Te_3}$ crystals is approximately 25 mW·cm⁻¹·K⁻¹ and gradually rises with a declining temperature, then decreases for 80 K. At room temperature, ZT is around 0.3, which is consistent with what has been observed for ordinary $\mathbf{Bi_2Te_3}$ (Figure 19).

Li et al. [146] examined the TE characteristics of two series of GR/Bi₂Te₃ composites that were made using a straightforward wet-chemical synthesis approach and sintering procedure. By ultrasonically dispersing a well-dispersed solution and vacuum filtering it, the GR sheets were evenly spread through the Bi₂Te₃ matrices. The most significant values were reached with a GR loading of 0.5 wt%. The power factors of the two types of GR/Bi₂Te₃ composites primarily rose with the growing GR content. They subsequently fell as the amount of GR in the mixture grew. Instead of the lower Sb coefficient values brought on by the reduction in n, this phenomenon was linked to the higher Sb coefficient values of the samples. A little addition of GR (up to 3 weight percent) was found to lower the thermal conductivity value because the GR surfaces produced many boundaries with the Bi₂Te₃ matrices, which served as efficient phonon scattering centers (Figure 20).

The GR/Bi₂Te₃-NW composite (1 wt%) had a maximum ZT value of 0.4 at approximately 26.85°C, which is higher than the Bi₂Te₃ NWs and GR/Bi₂Te₃-powder composites due to the enhanced power factor and lower *k* values. So, to summarize, our work has shown the advantages of integrating 1D Bi₂Te₃ NWs with GR as a possible means of developing highly effective TEMs (Figure 21).

Li *et al.* [146] found that the impact of monolayer GR's (G) presence on the conductivities of Bi₂Te₃ at the nano-

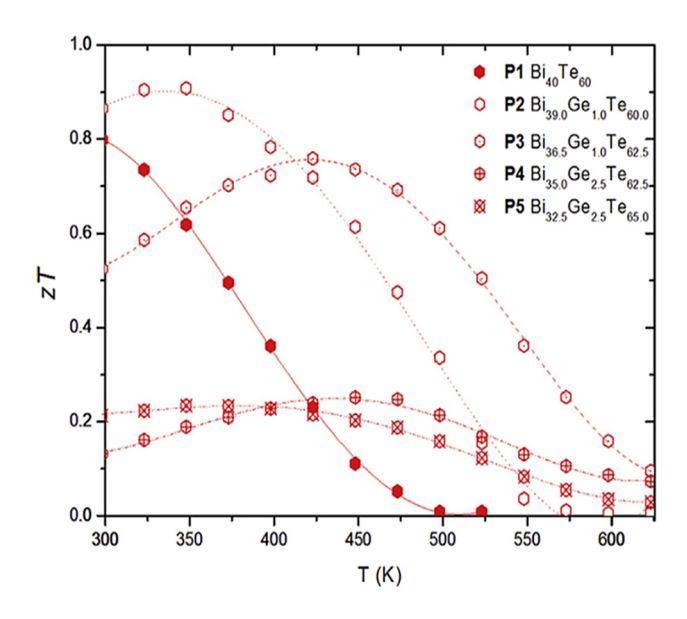


Figure 18: The ZT of $\mathbf{Bi}_{40-y}\mathbf{Ge}_{x}\mathbf{Te}_{60+x+y}$ with temperature, reproduced with the permission of Wu *et al.* [145].

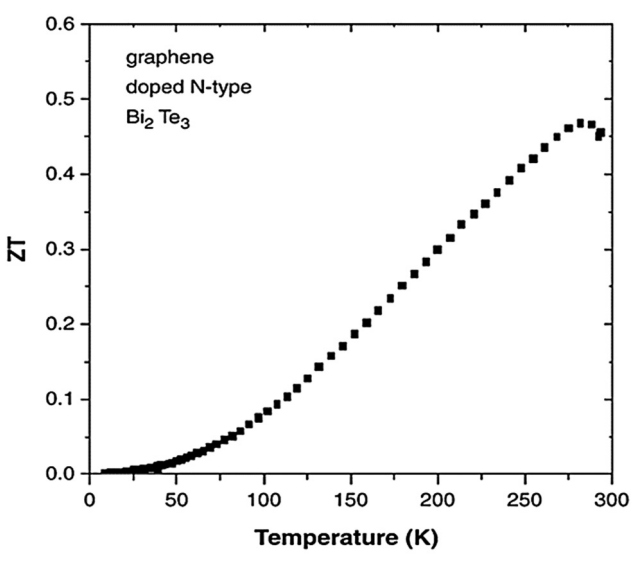


Figure 19: The ZT of Bi_2Te_3 :Gr samples, reproduced with the permission of [146].

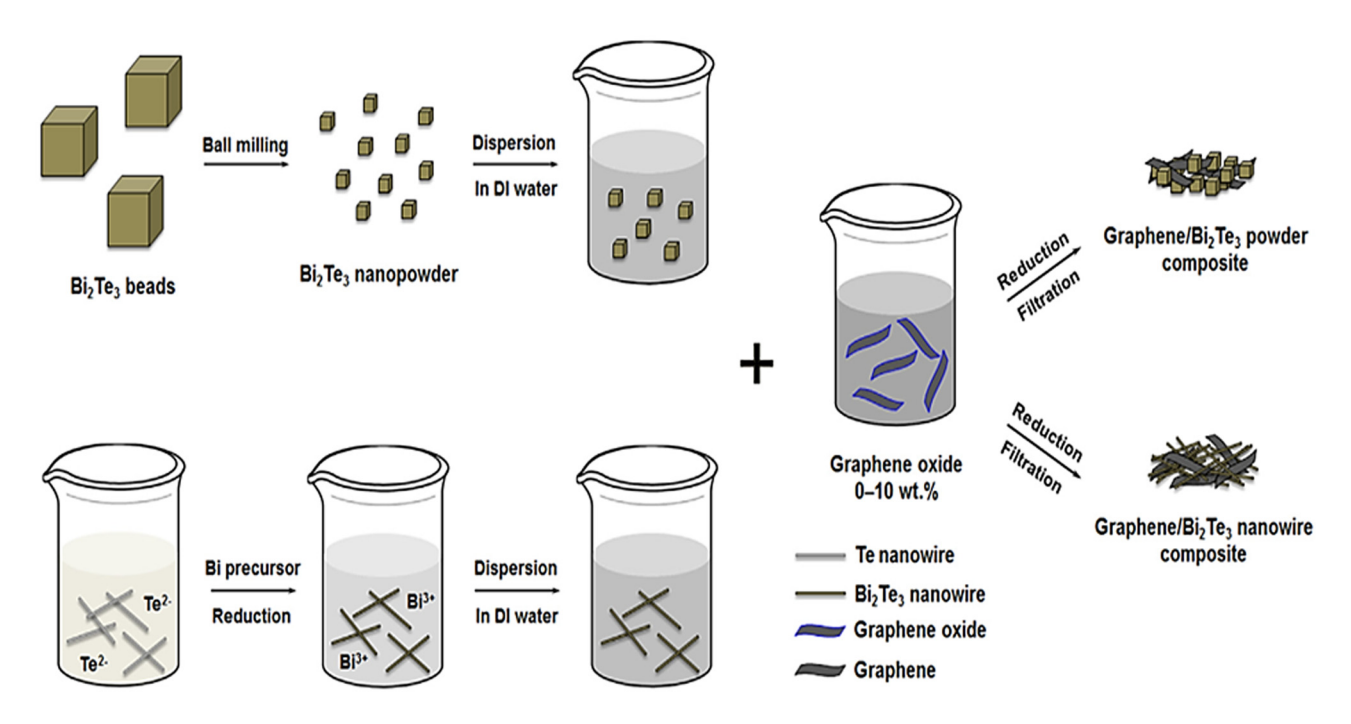


Figure 20: Diagram of the two separate GR/Bi₂Te₃ composites' production process, reproduced with the permission of Li et al. [146].

scale. Studies using conductive atomic force microscopy demonstrate that the addition of G causes electrical conductivity at Bi_2Te_3 :G contacts to decrease. The thermal conductivity and work function values of Bi_2Te_3 composites are different from those of the Bi_2Te_3 sample, as shown by the Kelvin probe and scanning thermal images. By testing the TE characteristics of Bi_2Te_3 and composites (temperature varies from 300 to 480 K), the reduction in thermal conductivity was further supported. The Bi_2Te_3 :G

composite sample's simultaneous rise in PF and reduction of thermal conductivity resulted in an improved ZT = 0.92 value. Due to the huge boundary area and two-dimensional behavior of G, the enhanced scattering of phonon and imperfect impact on electron transport are ascribed to the rise in ZT value. To establish the function of 2D materials in enhancing the TE properties, this work sheds light

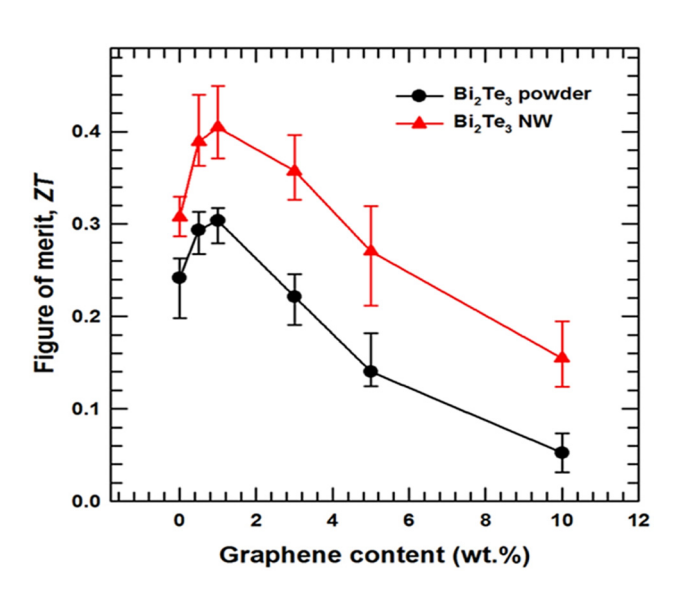


Figure 21: The ZT of ${\bf Bi_2Te_3}$:Gr samples *versus* varied GR content, reproduced with the permission of Li *et al.* [146].

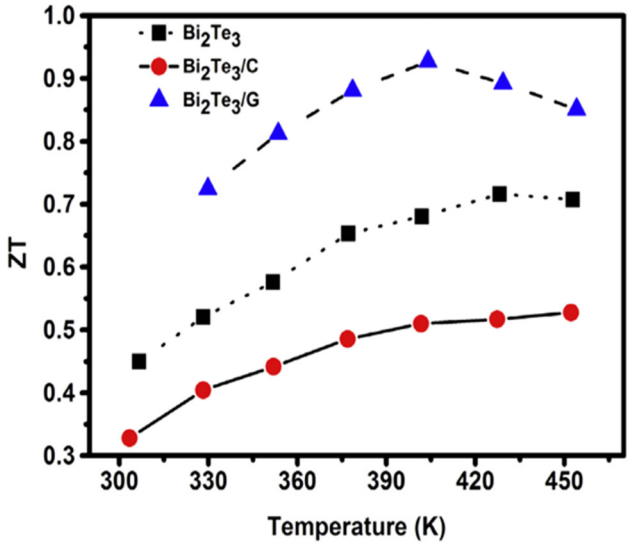


Figure 22: The ZT of **Bi₂Te₃**, **Bi₂Te₃/C**, and **Bi₂Te₃/G** samples *versus* varied temperatures, reproduced with the permission of Ju and Kim [147].

on a novel approach for straight nano-scale measurements of nano-composite samples (Figure 22).

5 Printable thermoelectric materials

Printing provides a possible means of producing TEMs at a cheaper cost and permits the creation of generators specifically designed to satisfy the needs of waste heat sources. The printing of TEMs has recently increased in terms of TE material and printing techniques, as well as performance with TEMs that are made commercially. According to Figure 23, at the proper temperatures, a ZT of 1 can produce efficiencies at the same level as those of other renewable technologies [211]. While renewable energy sources like wind and solar power are widely used in countries aiming to achieve carbon neutrality, TEs are only used in specialized fields like watches, space [212], or Peltier coolers [130]. It has been crucial from a technological standpoint to optimize the shape of TEGs composed of inorganic materials to increase their efficiency. The thermal-to-electrical conversion efficiencies are still far below the maximum Carnot efficiency, even if the TE characteristics of inorganic materials and the efficiency of their associated TEG have significantly increased. In addition, the conventional inorganic TE materials previously discussed have processability problems and are costly due to the presence of hazardous and rare

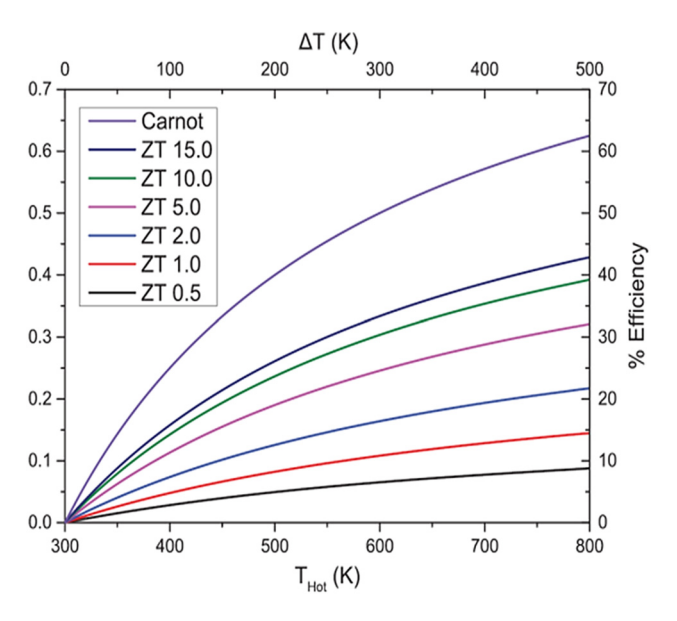


Figure 23: The ZT of different technologies, reproduced with the permission of Department for Business Energy & Industrial Strategy, Electricity Generation Costs [221].

elements. This may be somewhat explained by considering the high cost of producing TE devices, which goes toward the \$0.80 price tag for TE generators [213,214] as opposed to \$0.089 and \$0.084 for photovoltaic and wind turbines, respectively (price is per kW·h) [215].

The cost of producing TEG must be decreased, as must the price per kW·h of energy harvested if TEs are widely used. Reducing the price of producing TEMs is one technique to lower the cost of heat-to-electricity conversion. To create TEMs for modern marketable devices, spark plasma sintering, hot pressing, or a mixture of the two processes was used. These processes need expensive equipment, high temperatures, high pressures, and lengthy manufacturing periods. Contrarily, printing can be done in any environment, at high manufacturing rates, and with inexpensive tools. In recent years, printed thermoelectric has made substantial progress. Screen, inkjet, dispenser, and, more recently, 3D/pseudo-3D printing are some methods that have been researched (Figure 24). While not strictly categorized as a printing method, spin coating is frequently used in laboratories to measure the viability of ink mixtures before applying these inks in multiple printing methods. The center of a substrate that is stationary or rotating slowly has the ink formulation used on it. The substrate is programmed to turn rapidly once the ink has been put on it. Several spin velocities may be employed with different acceleration rates. When the procedure is followed correctly, consistent films are produced. This method's drawbacks include the need for a flat substrate, and only thin films are made. Traditionally used to create commercially printed items like posters and textiles, screen printing (Figure 23b) has recently gained new applications in the manufacture of printed circuit boards (PCBs) and other electrical goods [216-220]. Screen-printed electrodes are frequently employed in many industrial applications, including displays, radio frequency identification, solar cells, and sensors.

In traditional screen printing, a patterned stencil is affixed to the mesh, and a woven or stainless-steel mesh screen mask is used. Photolithography is used to create this stencil using a photo emulsion layer. An electrode design is deposited on the substrate through a stencil aperture, and conductive ink dispersed on the screen mask is squeezed into the woven or stainless-steel mesh. Ink is transferred to a substrate during the screen printing process, except for regions of the web that are impervious because of a hindering stencil. To fill the open holes on the screen with ink, a squeegee or blade is passed over it. After that, an opposite stroke lets the screen briefly trace the substrate along the contact line. As a result, the screen retracts when the blade has passed, causing the ink to moisten the substrate

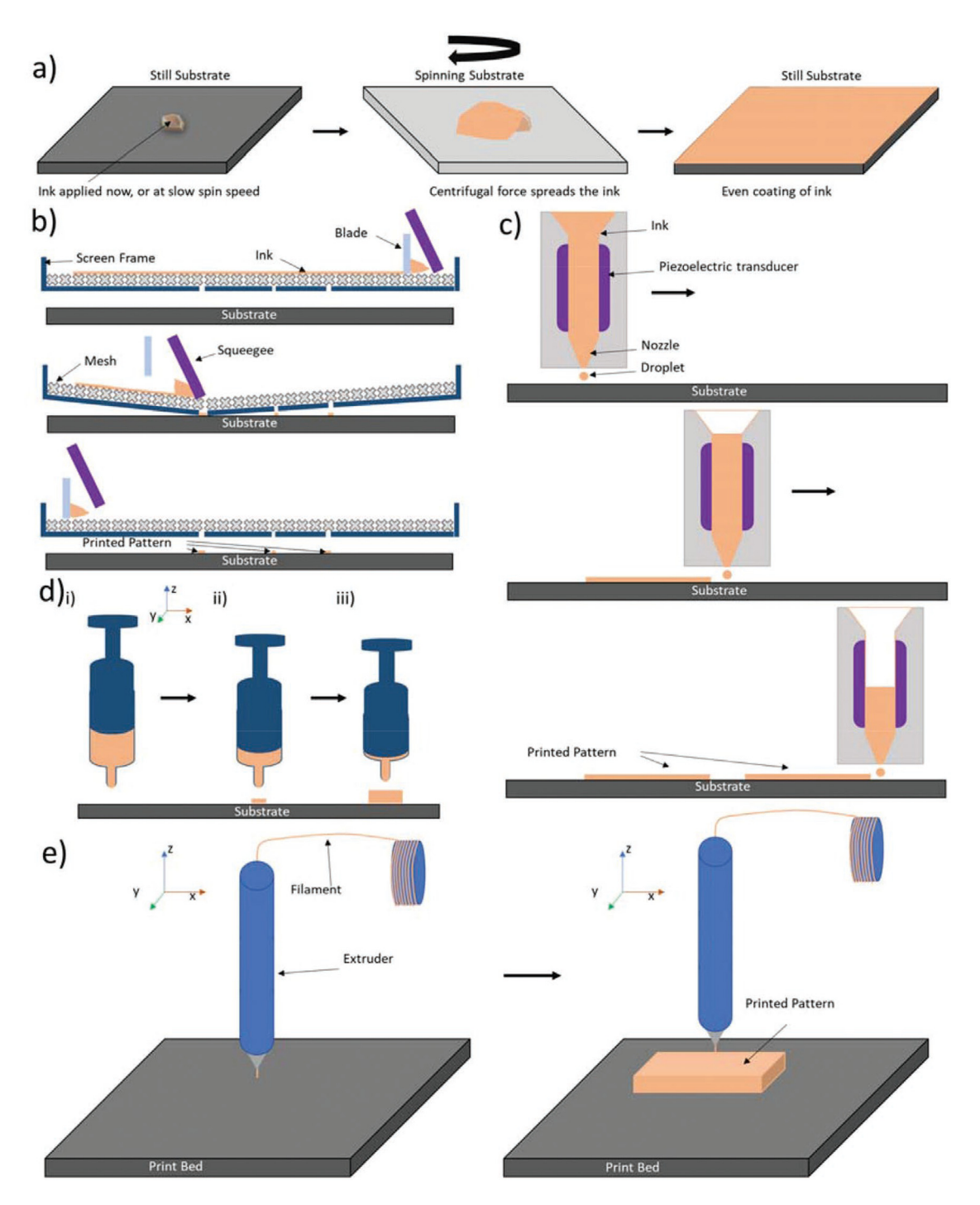


Figure 24: (a) Spin coating, (b) screen, (c) inkjet, (d) dispenser printing, and (e) fuse deposition modeling, reproduced with the permission of Department for Business Energy & Industrial Strategy, Electricity Generation Costs [221].

and be drawn out through mesh apertures. Various widths can be printed from a few microns to several hundred microns. Any level solid substrate can be utilized, and typical examples include polyimide for thermoelectric applications and aluminum, glass, and other common materials. Another constraint is the drying method, which might cause

contraction and surface irregularity, which may result in errors or imperfections in the ultimate product. If complicated pieces are required, the restriction on feature size may cause problems in the top product. Even though the inks can have various viscosities, more excellent viscosity inks are more commonly employed than those used in other printing

procedures [222,223]. Due to oxidation of the surface of films and the fact that the TE particles are not in liquid form, films made using this technique often exhibit reduced electrical conductivity, making electrical paths more challenging to cross [224,225]. The inkjet printing process entails the construction of an image on a substrate drop by drop while being electronically operated. One of the most promising techniques for the simple, low-cost production of high-resolution functional materials is inkjet printing technology. The liquid droplet transfer of ink material to a substrate is crucial to inkjet printing. As a result, there is no need for mechanical contact between the print head and the substrate [226]. The most common kind is drop-on-demand (DOD), with continuous inkjet printing as an alternative.

A voltage-activated piezoelectric diaphragm pushes ink into a chamber in a DOD system. When the diaphragm contracts due to a voltage change, there is a higher pressure inside the diaphragm than in the printing chamber. This pressure difference forces ink into the chamber. To print more ink on the subsequent initiation of the piezoelectric diaphragm, the capacity of the diaphragm diminishes when the voltage is reversed to let in air. There is minimal ink waste since ink droplets are only created when necessary. However, if the ink particle size is close to the nozzle diameter in inkjet printing, the printer head is prone to blockage and disfigurement [227]. If a bigger spout diameter is used, the image quality might be decreased [228]. Thus, research into these variables is essential to the development of functional material inkjet printing. Some applications require creating narrow, smooth structures with various geometries, such as integrated circuits and optical waveguides. Increasing printing resolution is a complex undertaking that necessitates an additional technological advancement related to the resource-intensive substrate pretreatment.

5.1 Printed TEDs

The n- and p-type components are linked in series in alternating patterns in the fundamental construction of TEDs such that the voltage created by each component sums up [229]. The output demand and the application determine how many elements are needed. Kim made a flexible TE generator on glass textiles using the screen-printing method. They bent the device to study its adaptability and showed that it maintained a constant efficiency even after 120 iterations [230]. With eight n-type Bi_2Te_3 and p-type Sb_2Te_3 thermocouples, they were able to fabricate printed films with a high power density at the temperature of 50 K and an open-circuit voltage of 0.09 V. They emphasized

how lightweight their product was. In addition, the device's output power on glass fabric was more significant than it was on Al_2O_3 substrates because the fabric has a small thermal resistance. Rösch *et al.* created a TE generator using screen printing, folding, and TE inks of PEDOT nanowires for the ptype and TiS_2 for n-type material for legs. They achieved a $47.8 \, \text{W} \cdot \text{cm}^{-2}$ power output at a $30 \, \text{K}$ temperature differential [231].

The item has 254 p and 253 n-type legs with an area of approximately 44.2854 mm² for each leg, arranged in a checkerboard design with a 39 cross-13 matrix. In their research, they employed a folding technique that allowed for a minimal spacing among the TE legs, or effectively the substrate thickness of 0.06 m, to act as an insulating barrier between the TE components. They attained a high thermocouple density of around 190 cm², which led to a high opencircuit voltage. Sb₂Te₃ and Bi₂Te₃ nanoparticles were used together with the screen-printing technique by Rösch et al. [232] to create a TEG, which was then infiltrated with PED-OT:PSS in DMSO at a 5 vol% concentration. DMSO aids in raising the materials. They showed that because printed nand p-type TE legs have distinct thermal and electrical characteristics, it affects how well the TEDs work. When n- and p-type TE's cross-sectional area ratio was 3, they attained a peak output power density of 1.2 × 10³ W·cm⁻² at 50°C ΔT with a hot surface temperature of approximately 59.85°C. Here, the flexible substrate for the printed TEG was a polyimide film with seven thermocouples, and the electrode was a screen-printed Ag film. With the help of body heat, their 15 TE couple-equipped device produced 0.0121 V voltage. In a 5 cm × 5 cm screen-printed TEG, We et al. [233] attained a peak output power of 0.2 kW at a ΔT of 43°C.

To create the TEG, they combined a hybrid Bi₂Te₃-polyimide ink with an ionic liquid. The hybrid Bi₂Te₃/PVA composite was chemically treated by Kato et al. [234] to create a screen-printed TEG with 10 stripes, each 2 mm and 25 mm wide. The displayed power output of TEG is up to 9 W·cm⁻² at a ΔT of 46°C. When there was a 50 K temperature differential between a printed TEG's hot and cold sides. Pires et al. [235] showed a power density of $2.7 \times 10^3 \,\mathrm{W \cdot cm^{-2}}$. The TEG was created using Bi₂Te_{2.7}Se_{0.3} films that were aerosol jet printed. They also performed experiments using tellurium-based nano solder and ball-milled Bi_{0.4}Sb_{1.6}Te₃ NPs. With ΔT of 80°C, the screen-printed device with four legs provided a significantly enhanced power density of $1.88 \times 10^3 \,\mathrm{W \cdot cm}^{-2}$. To create their device, Saeidi et al. also employed Bi₂Te₃ ink with a 12-weight percent Te-based nano-solder [236]. It had screen printing and was 10 mm \times 5 mm \times 166 m. At a ΔT of 105°C, they got a maximum output power density of $3.26c \times 10^3 \,\mathrm{W \cdot cm^{-2}}$. To create a

printed TEG, Varghese *et al.* [237] combined reduced-graphene oxide (RGO) nano-sheets with $\mathrm{Bi_2Te_3}$ nano-plates as ink. When the relative concentration of RGO in the ink was 1%, the greatest power production of 1.72 W at ΔT 20°C was observed. Any increase or decrease in RGO had a negative impact on power output. The power output of a printed TEG at a temperature differential of 20°C with a power density of 75 W·cm⁻² was reported by Ding *et al.* [238], who created TEGs at a millimeter size. On a polyimide substrate, they used dispenser printing to realize a TEG using $\mathrm{Sb_2Te_3}$ and $\mathrm{Bi_2Te_3}$ inks. They used n-type $\mathrm{Bi_2Te_3}$ -epoxy composite films with 1% Se and 62 single-legged printed TEG prototypes to produce a greater output of 130 W·cm⁻² at the same ΔT [239].

Madan *et al.* [240] created an n-type $\rm Bi_2Te_3$ ink and through screen-printing techniques made a TEG. With a ΔT 60°C, a power output density of 4,100 W·cm⁻² was obtained. The TEG comprised 0.5 nm n-type legs with a cross-sectional area of 0.02 mm². When 0.02 A of applied current was used, Varghese *et al.* [241] developed a cooling device and found a peak ΔT of 1.4°C. They produced a 6.2°C differential between the hot and cold sides when the current was raised to 60 mA. The highest result was 17.9°C at 180 A current. They discover that the Joule heating effect brought on by the device's internal resistance significantly impacts the temperature differential between the two

different temperature sides. The Peltier effect predominates when the applied current is small, and the cold side temperature drops due to the joule and Fourier effect, however, caused more heat to be produced when a high current was supplied. As a result, the cold side's temperature began to rise, and no net temperature of the cold surface was seen. Table 5 presents some of the TEMs and schemes used for printing.

6 Summary and perspectives

Despite significant progress in printed TEMs over the past 10 years, the effectiveness of printed TEDs still falls short of the capabilities of the materials they are made from. High electrical and thermal contact resistances primarily cause low conversion efficiency at the device level. In addition, most TE inks fall short in printability and mechanical properties, even though a few reports demonstrate good results [242,243]. One of the main problems is simultaneously improving the printed materials' mechanical and TE characteristics. Another obstacle to overcome is to make the preparation process simpler. Although its morphology is poor, solid-state processing at high temperatures enables a well-controlled chemical composition [244]. In addition,

Table 5: Summary of the power outputs of printed TEG based on Te

Materials	Printing method	Substrate	Thickness (mm)	Power (μW)	Power density (mW·cm ⁻²)	Cure <i>T</i> (K)
Sb ₂ Te ₃ /Bi _{1.8} Te _{3.2}	Screen	Kapton	0.067	0.048	180	523
Sb ₂ Te ₃ /Bi ₂ Te ₃	Screen	Glass Fabric	0.5	_	_	803
Sb ₂ Te ₃ /BiTe (epoxy)	Screen	Polyimide	0.078	0.44	180	523
$Bi_{0.5}Sb_{1.5}Te_3/Bi_2Te_{2.75}Se_{0.25}$ with epoxy	Dispenser	Free standing	4.4	0.126	_	_
BiSbTe/BiSeTe	Screen	a-Si quartz/SiO ₂	0.65	76,480	_	_
Bi _{0.5} Sb _{1.5} Te ₃ /Bi with epoxy	Dispenser	Glass	_	130	720	523
Sb ₂ Te ₃ /Bi ₂ Te ₃ (epoxy)	Dispenser	Polyimide	0.12	0.85	_	473
Sb ₂ Te ₃ /Bi ₂ Te ₃ with epoxy	Dispenser	Polyimide/glass	0.2	10.5	_	523
Bi ₂ Te ₃ (PVA)	Shadow Mask	PET	0.265	_	120	353
Bi ₂ Te ₃ with epoxy	Dispenser	Polyimide	0.1-0.12	25	720	623
BiTeSe with aterpineol and Disperbyk – 110	Screen	Polyimide	0.1	0.004	45	703
Sb _{1.5} Bi _{0.5} Te ₃ /Bi ₂ Te _{2.7} Se _{0.3}	Inkjet	Glass/Polyimide	150 layers	341	673	673
$Bi_{0.55}Sb_{1.45}Te_3/Bi_2Te_{2.7}$ with $Sb_2Te_4^2$	3D	N/A	0.35	2.8	723	723
$Bi_{0.4}Sb_{1.6}Te_3/Bi_2Te_{2.7}Se_{0.3}$ with Sb_2Te_3	3D	N/A	1.5-2.0	1,620	723	723
Se doped Bi ₂ Te ₃ with epoxy	Dispenser	Polyimide	0.2	1.6	720	523
$Pb_{0.98}Na_{0.02}Te/Pb_{0.98}Sb_{0.02}Te$	3D	N/A	2	216,300	3,150	373-1,023
$Bi_{0.4}Sb_{1.6}Te_3/Bi_2Te_{2.7}Se_{0.3}$	Laser	$Bi_{0.4}Sb_{1.6}Te_3$	1.6	1,450,000	1,440	673
$Bi_{0.5}Sb_{1.5}Te_3/Bi_2Te_3$	Inkjet	Polyimide	0.0015	0.127	723	723
Bi _{0.5} Sb _{1.5} Te ₃ /Bi with epoxy	Dispenser	Glass	_	130	720	523

higher temperatures cause the polymer substrates to break down. To increase the conversion efficiency of printed TED's, further in-depth research on device designs, electrical contacts, and thermal contacts is needed. New types of highefficiency printed TEMs may result from further study. Using fresh, efficient manufacturing techniques might enhance the performance and robustness of the TEDs.

In the past few years, it has been discovered that the photonic curing [245] procedure is an exceptional sintering method that enables excellent efficiency and mechanical flexibility. The procedure minimizes the possibility of oxidation because it only needs a few multiples of 10⁻³ s printed TEM's sintering. The shape of the TEDs also affects the conversion efficiency since it regulates the devices' electrical and thermal impedance [246]. Another crucial area of research is the impact of shape on device efficiency. One of the potential production techniques for ink creation is the solution-based wet chemistry approach, which enhances the ink's surface chemistry [247]. Significant findings from TE inks [248,249] and printed systems [250-254] made with various concentrations and recipes have been published recently. However, further study on the subject is required to overcome the challenges. While Te helps to improve TE characteristics, some of the commonly used dopants are very harmful to the environment. For the bulk manufacture of the TEDs, substitutes like p-type and n-type [255] might be created. Given the potential for printed TEs in various applications, the field will likely see much exploration in the coming years.

To make the TE technology feasible and affordable, a shift in thinking from traditional bulk to printable TEs has been widely noted in recent years. In addition, bulk TEs do not provide shape conformity, which is necessary for numerous applications on irregular surfaces. Shape-conformable TEDs might be produced at a reasonable cost thanks to the printed TEs. To begin with, organic polymers have been the focus of efforts to transform them into powerful printed TEMs. Their low TE efficiency, however, restricts their use despite their good printing ability. Inorganic-based printed TEs have recently made advancements, as detailed in this article. Inorganic materials that can be printed provide a way around these restrictions. We have outlined the basic principles of TEs, the composition of TE ink, and current developments in inorganic and hybrid printed TE materials. Inorganic TEM materials have been the focus of most studies on printed TEs. However, other chalcogenides have also demonstrated promising abilities. However, improving TE efficiency by hybridizing organic and inorganic materials could be fruitful. There are several reasons for the competitiveness of TEDs compared with other renewable energy resources, including efficiency in

waste heat recovery, low maintenance and long lifespan, scalability and flexibility, reliability and durability, low environment impact, diversified energy sources, technological innovation, and cost reduction. These findings might open the door for the production of low-cost TEDs.

Acknowledgments: The authors acknowledge financial support by the Project of State Key Laboratory of Environment-Friendly Energy Materials (227/35100011).

Funding information: This work was partly financially supported by the Project of State Key Laboratory of Environment-Friendly Energy Materials (227/35100011).

Author contributions: Writing – original draft preparation; conceptualization, funding acquisition by Syed Irfan, review – Zhiyuan Yang and supervised and edited by Sadaf Bashir Khan. All authors have accepted responsibility for the entire content of this manuscript and approved its submission.

Conflict of interest: The authors state no conflict of interest.

Data availability statement: The datasets generated and/ or analyzed during the current study are available from the corresponding author on reasonable request.

References

- Seebeck, T. J. Magnetische polarisation der metalle und erze durch temperatur differenz. *Annalen der Physik*, Vol. 82, No. 2, 1822. pp. 133–160.
- [2] Peltier, J. C. A. Nouvelles Expériemences sur la Caloricite descourants électriques. *Annales de Chimie et de Physique*, Vol. 56, 1834, pp. 371–386.
- [3] Thomson, W. On a mechanical theory of thermoelectric currents. Proceedings of the Royal Society of Edinburgh, Vol. 3, 1851, pp. 91–98.
- [4] Wei, Q., S. Qianfa, L. YiZhen, C. Rui, G. Xiuying, Z. Tixian, et al. Ultrathin elementary te nanocrystalline films prepared by pure physical method for NO_2 detection. *Journal of Electronic Materials*, Vol. 52, 2022, pp. 1900–1907.
- [5] Chen, L., R. Liu, and X. Shi. *Thermoelectric materials and devices*, Shanghai Institute of Ceramics, Chinese Academy of Sciences, Shanghai, China, 2020.
- [6] Indraneel, N. and N. Milankumar. Modeling and validation of the impact of electric current and ambient temperature on the thermoelectric performance of lithium-ion batteries. *Energy Technology*, Vol. 13, No. 2, 2021, id. 2100774.
- [7] Wanli, Y., L. Jinxi, and H. Yuantai. Mechanical tuning methodology on the barrier configuration near a piezoelectric PN interface and the regulation mechanism on I–V characteristics of the junction. *Nano Energy*, Vol. 81, 2020, id. 105581.

- [8] Costa, S. S. and L. C. Sampaio. Recent progress in the spin Seebeck and spin Peltier effects in insulating magnets. *Journal of Magnetism and Magnetic Materials*, Vol. 547, 2021, id. 168773.
- [9] Yamashita O. Effect of linear temperature dependence of thermoelectric properties on energy conversion efficiency. *Energy Convers Manag.* Vol. 49, No. 11, 2008, pp. 3163–3169.
- [10] Sandoz-Rosado E, Stevens RJ. Experimental characterization of thermoelectric modules and comparison with theoretical models for power generation. J Electron Mater. Vol. 38, 2009, pp. 1239–1244.
- [11] Kim HS, Liu W, Ren Z. Efficiency and output power of thermoelectric module by taking into account corrected Joule and Thomson heat. J Appl Phys. Vol. 118, 2015, id. 115103.
- [12] Kosuke, M., I. Yuki, and O. Koji. Achieving Carnot efficiency in a finite-power Brownian Carnot cycle with arbitrary temperature difference. *Physical Review E*, Vol. 105, 2022, id. 034102.
- [13] Ruihua, C., X. Weicong, D. Shuai, Z. Ruikai, C. Q. Siyoung, and Z. Li. A contemporary description of the carnot cycle featured by chemical work from equilibrium: The electrochemical carnot cycle. *Energy*, Vol. 280, 2023, id. 128168.
- [14] Tianye, W., L. Hu, F. Yangming, Z. Xiaoxiao, H. Long, and S. Aimin. A graphene-nanoribbon-based thermoelectric generator. *Carbon*, Vol. 210, 2023, id. 118053.
- [15] Ruo, J. W., H. P. Yu, and L. C. Wen. A dimensionless study on thermal control of positive temperature coefficient (PTC) materials. *International Communications in Heat and Mass Transfer*, Vol. 120, 2020, id. 104987.
- [16] Yang, F., X. Zhang, B. Yan, J. Lin, L. Liu, L. Tang, et al. Study of Seebeck coefficient in organic materials under nonlinear temperature distributions. *Modern Physics Letters B*, Vol. 37, No. 29, 2023. id. 2350102.
- [17] Dongxing, S., C. Cheng, A. Meng, D. Yanzheng, M. Weigang, W. Ke, et al. Ionic Seebeck coefficient and figure of merit in ionic thermoelectric materials. *Cell Reports Physical Science*, Vol. 3, No. 2, 2022. id. 101018.
- [18] Sonya, H., F. Eric, C. Benoit, P. Christophe, Z. Marcin, W. Ś. Dorota, et al. Composites between perovskite and layered Co-based oxides for modification of the thermoelectric efficiency. *Materials*, Vol. 14, 2021, id. 7019.
- [19] Edoardo, N., F. Walter, B. Paolo, and G. Alessandro. Leaky-wave analysis of TM-, TE-, and hybrid-polarized aperture-fed besselbeam launchers for wireless-power-transfer links. *IEEE Transactions on Antennas and Propagation*, Vol. 71, No. 2, 2022, pp. 1424–1436.
- [20] Weihua, W., W. Quanlin, S. Lin, J. Peng, and B. Xinhe. High-performance Sb₂Si₂Te₆ thermoelectric device. *Materials Today Energy*, Vol. 37, 2023, id. 101370.
- [21] Ibrahim, B. H., B. Zahia, and Z. Katir. Metal-based folded-ther-mopile for 2.5D micro-thermoelectric generators. Sensors and Actuators, A: Physical, Vol. 349, 2022, id. 114090.
- [22] Feng, Z., J. Chen, X. Deqiao, L. Bin, Q. Mingbo, Y. Xinyu, et al. Research on laser-assisted selective metallization of a 3D printed ceramic surface. RSC Advances, Vol. 10, 2020, pp. 44015–44024.
- [23] Panisara, S. and S. Phairote. Improvements in the properties of low-Ag SAC105 solder alloys with the addition of tellurium. *Journal* of Materials Science: Materials in Electronics, Vol. 34, 2023, id. 1327.
- [24] Zhang, Q. H., X. Y. Huang, S. Q. Bai, X. Shi, C. Uher, and L. D. Chen. Thermoelectric devices for power generation: recent progress and future challenges. *Advanced Engineering Materials*, Vol. 18, 2016, pp. 194–213.

- [25] Zhao, D., X. Li, L. He, W. Jiang, and L. Chen. Interfacial evolution behavior and reliability evaluation of CoSb₃/Ti/Mo-Cu thermoelectric joints during accelerated thermal aging. *Journal of Alloys* and Compounds, Vol. 477, 2009, pp. 425–431.
- [26] Li, F., X. Huang, W. Jiang, and L. Chen. Interface microstructure and performance of Sb contacts in bismuth telluride-based thermoelectric elements. *Journal of Electronic Materials*, Vol. 42, 2013, pp. 1219–1224.
- [27] Jianqiang, Z., W. Ping, Z. Huiqiang, L. Longzhou, Z. Wanting, N. Xiaolei, et al. Enhanced contact performance and thermal tolerance of Ni/Bi₂Te₃ joints for Bi₂Te₃-based thermoelectric devices. ACS Applied Materials & Interfaces, Vol. 15, No. 18, 2023, pp. 22705–22713.
- [28] Dariusz, B., C. Artur, and D. Grzegorz. Influence of the sintering method on the properties of a multiferroic ceramic composite based on PZT-type ferroelectric material and Ni-Zn ferrite. *Materials*, Vol. 15, No. 23, 2022, id. 8461.
- [29] Temel, V., G. Onur, B. A. Serhatcan, and C. A. Hüseyin. Novel advanced copper-silver materials produced from recycled dendritic copper powders using electroless coating and hot pressing. *Powder Metallurgy*, Vol. 65, 2022, pp. 390–402.
- [30] Smita, H., S. Gupta, R. Vasudevan, and K. Sachdev. Synthesis and characterization of doped Mg₂Si_{0.4}Sn_{0.6} thermoelectric material made in exclusion of glove box. *Solid State Communications*, Vol. 353, 2022, id. 114847.
- [31] Shengzhi, D., W. Yifan, W. Xiaowen, W. Meihua, W. Lianyi, F. Minghao, et al. Printable graphite-based thermoelectric foam for flexible thermoelectric devices. *Applied Physics Letters*, Vol. 123, 2023, id. 063904.
- [32] Jeong, S. Y., C. Seongyun, and H. I. Sang. Advances in carbon-based thermoelectric materials for high-performance. flexible thermoelectric devices. *Carbon Energy*, Vol. 3, No. 5, 2021, pp. 667–708.
- [33] Jiaqing, Z., C. Jiayi, C. Zhewei, L. Ya, Z. Jiye, S. Tao, et al. Printed flexible thermoelectric materials and devices. *Journal of Materials Chemistry A*, Vol. 9, 2021, pp. 19439–19464.
- [34] Yubing, X., T. Kechen, W. Jiang, H. Kai, X. Yani, L. Jianan, et al. High-performance wearable Bi₂Te₃-based thermoelectric generator. *Applied Sciences*, Vol. 13, No. 10, 2023, id. 5971.
- [35] Poonam, R. and P. P. Tripathy. Experimental investigation on heat transfer performance of solar collector with baffles and semicircular loops fins under varied air mass flow rates. *International Journal of Thermal Sciences*, Vol. 178, 2022, id. 107597.
- [36] Fuzhang, W., N. K. Rangaswamy, C. P. Ballajja, K. Umair, Z. Aurang, H. A. A. Abdel, et al. Aspects of uniform horizontal magnetic field and nanoparticle aggregation in the flow of nanofluid with melting heat transfer. *Nanomaterials*, Vol. 12, No. 6, 2022, id. 1000.
- [37] Nidhal, B. K., B. Nirmalendu, T. Hussein, I. M. Hayder, M. M. Jasim, K. I. Raed, et al. Geometry modification of a vertical shell-andtube latent heat thermal energy storage system using a framed structure with different undulated shapes for the phase change material container during the melting process. *Journal of Energy Storage*, Vol. 72, 2023, id. 108365.
- [38] Jiang, J. M., Y. L. Qing, F. L. Peng, Z. Ping, S. Biplab, O. Tao, et al. Ultralow thermal conductivity and anisotropic thermoelectric performance in layered materials LaMOCh (M = Cu, Ag; Ch = S, Se). Physical Chemistry Chemical Physics, Vol. 24, 2022, pp. 21261–21269.

- [39] Deepthi, J. K. Theoretical modeling of Perovskite–Kesterite Tandem solar cells for optimal photovoltaic performance. *Energy Technology*, Vol. 10, No. 12, 2022, id. 2200635.
- [40] Weinberg, F. J., D. M. Rowe, and G. Min. Novel high performance small-scale thermoelectric power generation employing regenerative combustion systems. *Journal of Physics D: Applied Physics*, Vol. 35, 2002, pp. L61–L63.
- [41] Juan, W., Y. Zhong, M. Zhijun, D. Hongbo, Z. Jiachen, T. Dong, et al. Effect of the addition of cerium on the microstructure evolution and thermal expansion properties of cast Al-Cu-Fe alloy. *Materials Research Express*, Vol. 8, No. 3, 2021, id. 036503.
- [42] Ya, G., L. Yousheng, H. Qing, W. Wenhao, C. Jiechao, and M. H. Si. Geometric optimization of segmented thermoelectric generators for waste heat recovery systems using genetic algorithm. *Energy*, Vol. 233, 2021, id. 121220.
- [43] Limei, S., W. Yupeng, T. Xiao, X. Shenming, and S. Yongjun. Inverse optimization investigation for thermoelectric material from device level. *Energy Conversion and Management*, Vol. 228, 2021, id. 113669.
- [44] Manuela, G., C. Flaviana, and M. Francesco. Numerical and experimental investigations of a novel 3D bucklicrystal auxetic structure produced by metal additive manufacturing. *Thin-Walled Structures*, Vol. 180, 2022, id. 109850.
- [45] Minghui, G., L. Zhenhua, W. Yeting, Z. Yulong, Z. Yu, W. Shixue, et al. Experimental study on thermoelectric power generation based on cryogenic liquid cold energy. *Energy*, Vol. 220, 2021, id. 119746.
- [46] Fan, C., H. Kun, G. Meng, Z. Yan, X. Wei, H. Juntao, et al. Magnetocaloric properties of melt-extracted Gd-Co-Al amorphous/crystalline composite fiber. *Metals*, Vol. 12, No. 8, 2022, id. 1367.
- [47] Crane, D. T. and L. E. Bell. Progress towards maximizing the performance of a thermoelectric power generator. In *2006 25th International Conference on Thermoelectrics*, IEEE, 2006, pp. 11–16.
- [48] Chen, L., R. Liu, and X. Shi. *Thermoelectric materials and devices*, 1st ed., Science Press, Beijing, 2018, p. 195.
- [49] Joohyun, L., H. K. Se, A. A. Raquel, K. Olga, P. C. Pyuck, T. S. Leigh, et al. Atomic scale mapping of impurities in partially reduced hollow ${\rm TiO_2}$ nanowires. *Angewandte Chemie*, Vol. 59, No. 14, 2020, pp. 5651–5655.
- [50] Jun, Y. C., H. C. Joon, C. Jacob, M. Y. Jong, and D. K. Il. Bias-free graphene solid cell to realize the real-time observation on dynamical changes of electrodes. *Advanced Materials Interfaces*, Vol. 10, No. 2, 2022, id. 2201849.
- [51] Wei, Z., Y. A. O. Shanshan, and W. Feng. In situ, operando lithium K-edge energy-loss spectroscopy of battery materials. *Microscopy and Microanalysis*, Vol. 26, No. S2, 2020, pp. 2538–2540.
- [52] Zhang, Q., J. Liao, Y. Tang, M. Gu, C. Ming, P. Qiu, et al. Realizing a thermoelectric conversion efficiency of 12% in bismuth telluride/ skutterudite segmented modules through full-parameter optimization and energy-loss minimized integration. *Energy & Environmental Science*, Vol. 10, 2017, pp. 956–963.
- [53] Shi, Y., N. Ni, Q. Ding, and X. Zhao. Tailoring high-temperature stability and electrical conductivity of high entropy lanthanum manganite for solid oxide fuel cell cathodes. *Journal of Materials Chemistry A*, Vol. 10, 2022, pp. 2256–2270.
- [54] Cushing, B. L., V. L. Kolesnichenko, and C. J. O'connor. Recent advances in the liquid-phase syntheses of inorganic nanoparticles. *Chemical Reviews*, Vol. 104, No. 9, 2004, pp. 3893–3946.

- [55] Wu, M., G. Lin, D. Chen, G. Wang, D. He, S. Feng, et al. Solhydrothermal synthesis and hydrothermally structural evolution of nanocrystal titanium dioxide. *Chemistry of Materials*, Vol. 14, No. 5, 2002, pp. 1974–1980.
- [56] Hakuta, Y., H. Ura, H. Hayashi, and K. Arai. Continuous production of BaTiO₃ nanoparticles by hydrothermal synthesis. *Industrial & Engineering Chemistry Research*, Vol. 44, No. 4, 2005, pp. 840–846.
- [57] Rabenau, A. The role of hydrothermal synthesis in preparative chemistry. Angewandte Chemie, International Edition in English, Vol. 24, No. 12, 1985, pp. 1026–1040.
- [58] Shuangming, S., X. Chaoyi, L. Heping, X. Liping, L. Sen, and L. Shengbin. In situ electrical conductivity measurements of porous water-containing rock materials under high temperature and high pressure conditions in an autoclave. *Review of Scientific Instruments*, Vol. 92, No. 9, 2021, id. 095104.
- [59] Shi, W., S. Song, and H. Zhang. Hydrothermal synthetic strategies of inorganic semiconducting nanostructures. *Chemical Society Reviews*, Vol. 42, No. 13, 2013, pp. 5714–5743.
- [60] Cundy, C. S. and P. A. Cox. The hydrothermal synthesis of zeolites: precursors, intermediates and reaction mechanism. *Microporous and Mesoporous Materials*, Vol. 82, No. 1, 2005, pp. 1–78.
- [61] Jiao, X., D. Chen, and L. Xiao. Effect of organic additives in hydrothermal zirconia nanocrystallites. *Journal of Crystal Growth*, Vol. 258, 2023, id. 158.
- [62] Sun, C., H. Li, H. Zhang, Z. Wang, and L. Chen. Controlled synthesis of CeO₂ nanorods by a solvothermal method. Nanotechnology, Vol. 16, 2005, id. 1454.
- [63] Wang, G., Z. Wang, Y. Zhang, G. Fei, and L. Zhang. Controlled synthesis and characterization of large-scale, uniform Dy(OH)₃ and Dy₂O₃ single-crystal nanorods by a hydrothermal method. *Nanotechnology*, Vol. 15, 2004, id. 1307.
- [64] Sorescu, M., L. Diamandescu, M. D. Tarabasanu, and V. S. Teodorescu. Nanocrystalline rhombohedral In₂O₃ synthesized by hydrothermal and postannealing pathways. *Journal of Materials Science*, Vol. 39, 2004, id. 675.
- [65] Jing, Z. and S. Wu. Synthesis and characterization of monodisperse hematite nanoparticles modified by surfactant via hydrothermal approach. *Materials Letters*, Vol. 58, 2004, id. 3637.
- [66] Zheng, Y., Y. Cheng, Y. Wang, and F. Bao. Synthesis and shape evolution of alpha-Fe₂O₃ nanophase through two-step oriented aggregation in solvothermal system. *Journal of Crystal Growth*, Vol. 284, 2005, id. 221.
- [67] Li, G. S., J. R. L. Smith, H. Inomata, and K. Arai. Preparation and magnetization of hematite nanocrystals with amorphous iron oxide layers by hydrothermal conditions. *Materials Research Bulletin*, Vol. 37, 2002, id. 949.
- [68] Suber, L., D. Fiorani, P. Imperatory, S. Foglia, A. Montone, and R. Zysler. Effects of thermal treatments on thermal on structural and magnetic properties of acicular alpha-Fe₂O₃ nanoparticles. *Nanostructured Materials*, Vol. 11, 1999, id. 797.
- [69] Cote, L. J., A. S. Teja, A. P. Wilkinson, and Z. J. Zhang. Continuous hydrothermal synthesis of CoFe₂O₃ nanoparticles. *Fluid Phase Equilibria*, Vol. 210, 2003, id. 307.
- [70] Cote, L. J., A. S. Teja, A. P. Wilkinson, and Z. J. Zhang. Continuous hydrothermal synthesis and crystallization of magnetic oxide nanoparticles. *Journal of Materials Research*, Vol. 17, 2002, id. 2410.
- [71] Wan, J., X. Chen, Z. Wang, X. Yang, and Y. T. Qian. A soft-templateassisted hydrothermal approach to single crystal Fe₂O₄ nanorods. *Journal of Crystal Growth*, Vol. 276, 2005, id. 571.

- [72] Kominami, H., M. Miyakawa, S. Murakami, T. Yasuda, M. Kohno, S. Onoue, et al. Solvothermal synthesis of tantalum (v) oxide nanoparticles and their photocatalytic activities in aqueous suspension system. Physical Chemistry Chemical Physics, Vol. 3, 2001, pp. 2697-2703.
- Adschiri, T., K. Kanaszawa, and K. Arai. Rapid and continuous hydrothermal crystallization of metal oxide particles in supercritical water. Journal of the American Ceramic Society, Vol. 75, 1992,
- Adschiri, T., K. Kanaszawa, and K. Arai. Rapid and continuous hydrothermal synthesis of boehmite particles in subcritical and supercritical water. Journal of the American Ceramic Society, Vol. 75,
- [75] Hakuta, Y., T. Adschiri, T. Suzuki, T. Chida, K. Seino, and K. Arai. Flow method for rapidly producing barium hexaferrite particles in supercritical water. Journal of the American Ceramic Society, Vol. 81, 1998. id. 2461.
- [76] Adschiri, T., Y. Hakuta, K. Sue, and K. Arai. Hydrothermal synthesis of metal oxide nanoparticles at supercritical conditions. Journal of Nanoparticle Research, Vol. 3, 2001, id. 227.
- Hakuta, Y., S. Onai, H. Terayama, T. Adschiri, and K. Aria. [77] Production of Ultra-fine ceria particles by hydrothermal synthesis under supercritical conditions. Journal of Materials Science Letters, Vol. 17, 1998, id. 1211.
- [78] Byrappa, K., R. K. M. Lokanatha, and M. Yoshimura. Hydrothermal preparation of TiO₂ and Photocatalytic degradation of hexacholocyclohexane and dicholorodiphenyltricholorometane. Environmental Technology, Vol. 21, 2000, id. 1085.
- [79] Liu, Y., Y. Du, Q. Meng, J. Xu, and S. Z. Shen. Effects of preparation methods on the thermoelectric performance of SWCNT/Bi₂Te₃ bulk composites. Materials, Vol. 13, No. 11, 2020, id. 2636.
- Niederberger, M. and N. Pinna. Metal oxide nanoparticles in organic solvents: Synthesis, formation, assembly and application (Engineering Materials and Processes), Springer, Berlin, Germnay, 2009.
- [81] Feinle, A., M. S. Elsaesser, and N. Huesing. Sol-gel synthesis of monolithic materials with hierarchical porosity. Chemical Society Reviews, Vol. 45, No. 12, 2016, pp. 3377-3399.
- [82] Liao, Y., Y. Xu, and Y. Chan. Semiconductor nanocrystals in sol-gel derived matrices. Physical Chemistry Chemical Physics, Vol. 15, No. 33, 2013, pp. 13694-13704.
- [83] Owens, G. J., R. K. Singh, F. Foroutan, M. Alqaysi, C. M. Han, C. Mahapatra, et al. Sol-gel based materials for biomedical applications. Progress in Materials Science, Vol. 77, 2016, pp. 1-79.
- Haruta, M. Nanoparticulate gold catalysts for low-temperature CO oxidation. Journal of New Materials for Electrochemical Systems, Vol. 7, 2004, pp. 163-172.
- [85] Tian, N., Z. Y. Zhou, S. G. Sun, Y. Ding, and Z. L. Wang. Synthesis of tetrahexahedral platinum nanocrystals with high-index facets and high electro-oxidation activity. Science, Vol. 316, No. 5825, 2007, pp. 732-735.
- Xu, R., D. Wang, J. Zhang, and Y. Li. Shape-dependent catalytic [86] activity of silver nanoparticles for the oxidation of styrene. Chemistry - An Asian Journal, Vol. 1, No. 6, 2006, pp. 888-893.
- [87] Rahman, I. A. and V. Padavettan. Synthesis of silica nanoparticles by sol-gel: size-dependent properties, surface modification, and applications in silica-polymer nanocomposites - a review. Journal of Nanomaterials, Vol. 15, 2012, id. 2012.
- Benjamin, B., M. Julius, S. Simon, I. Suzylawati, A. Z. Nor, N. A. J. Siti, et al. Catalysis of silica sol-gel reactions using a PdCl₂

- precursor. Journal of Sol-Gel Science and Technology, Vol. 95, 2020, pp. 456-464.
- [89] Jolanta, N., M. P. Joanna, R. Andrzej, and S. Maciej. Spectroscopic and rheological investigation of candidates for the doublelayered binder for amorphous metal ribbon. Journal of Molecular Structure, Vol. 1207, 2020, id. 127763.
- Paolo, V., C. Elena, S. C. Özgür, B. Giovanni, and L. Cristina. Procedure to generate a selection chart for microwave sol-gel synthesis of nanoparticles. Chemical Engineering and Processing: Process Intensification, Vol. 189, 2023, id. 109383.
- [91] Ashraf, M. A., A. M. Ruaa, J. A. Mohammed, and A. A. T. Wesam. Dispersion of pure silica xerogel vs NaYF4- xerogel nanomaterials in silica aerogel and their effect on the optical and structural properties. Optical Materials, Vol. 118, 2021, id. 111274.
- Bowen, Z., G. Qing, D. Bushi, W. Nan, D. Yuxiang, and Q. Yang. [92] Quality optimization of Bi2212 films prepared by aqueous solvent sol-gel method with nonionic surfactants. Ceramics International, Vol. 48, No. 24, 2022, pp. 36845-36852.
- [93] Ra, B. G., D. Mukherjee, and B. M. Reddy. Novel approaches for preparation of nanoparticles. In Nanostructures for Novel Therapy, Elsevier, CSIR-Indian Institute of Chemical Technology, Hyderabad, India, 2017, pp. 1-36.
- [94] Bradley, D., R. C. Mehrotra, I. Rothwell, and A. Singh. Alkoxo and aryloxo derivatives of metals, Academic Press, New York, 2001.
- [95] Turova, N. Y., E. P. Turevskaya, V. G. Kessler, and M. I. Yanovskaya. The chemistry of metal alkoxides, Springer Science+Business Media, New York, 2002.
- [96] Corriu, R. J. and D. Leclercq. Recent developments of molecular chemistry for sol-gel processes. Angewandte Chemie, International Edition in English, Vol. 35, No. 13-14, 1996, pp. 1420-1436.
- [97] Aman, K., Chitoria, M. Arshid, and M. A. Shah. A review of ZrO₂ nanoparticles applications and recent advancements. Ceramics International, Vol. 49, No. 20, 2023, pp. 32343-32358.
- [98] Maryam, H., M. D. Mohammad, M. M. Seyed, and B. Ali. Morphology and phase-controlled growth of CuInS₂ nanoparticles through polyol based heating up synthesis approach. Materials Science in Semiconductor Processing, Vol. 121, 2021, id. 105401.
- [99] Carroll, K. J., J. U. Reveles, M. D. Shultz, S. N. Khanna, and E. E. Carpenter. Preparation of elemental Cu and Ni nanoparticles by the polyol method: an experimental and theoretical approach. The Journal of Physical Chemistry C, Vol. 115, No. 6, 2011, pp. 2656-2664.
- Adschiri, T., Y. Hakuta, and K. Arai. Hydrothermal synthesis of metal oxide fine particles at supercritical conditions. Industrial & Engineering Chemistry Research, Vol. 39, 2000, id. 4901.
- [101] Grisaru, H., O. Palchik, A. Gedanken, V. Palchik, M. A. Slifkin, and A. M. Weiss. Microwave-assisted polyol synthesis of CuInTe₂ and CuInSe₂ nanoparticles. Inorganic Chemistry, Vol. 42, No. 22, 2003, pp. 7148-7155.
- [102] Kaixuan, Z., Y. Zhijie, W. Huiying, G. Jinxin, Y. Yanzhao, and W. Jingjing. Controlled syntheses of monodispersed metal oxide nanocrystals from bulk metal oxide materials. CrystEngComm, Vol. 22, 2020, pp. 4790-4796.
- [103] Riyang, S., L. Rongxuan, L. Biqin, L. Bowen, and T. Zhipeng. High dispersed Ru/SiO₂-ZrO₂ catalyst prepared by polyol reduction method and its catalytic applications in the hydrodeoxygenation of phenolic compounds and pyrolysis lignin-oil. Fuel, Vol. 265, 2020, id. 116962.

- [104] May, A. F., J. Yan, and M. A. McGuire. A practical guide for crystal growth of van der Waals layered materials. Journal of Applied Physics, Vol. 128, No. 5, 2020, id. 051101.
- [105] Wang, X. and N. Ma. Bridgman-stockbarger growth of binary alloyed semiconductor crystals with steady magnetic fields. Journal of Thermophysics and Heat Transfer, Vol. 20, No. 2, 2006, pp. 313-319.
- Kürten, M. and I. Schilz. Czochralski growth of SitGe1-x single crystals. Journal of Crystal Growth, Vol. 139, No. 1-2, 1994, pp. 1-5.
- [107] Liu, Y., X. Guo, N. Xia, Z. Hong, H. Zhang, and D. Yang. Floating particles in the melt during the growth of β-Ga₂O₃ single crystals using the Czochralski method. Metals, Vol. 12, No. 7, 2022, id. 1171.
- [108] Qijiang, S., H. Pengru, Y. Fuhua, Y. Linjing, and L. Chen. Study on crystal growth of Ge/Si quantum dots at different Ge deposition by using magnetron-sputtering technique. Scientific Reports, Vol. 13, 2023, id. 7511.
- [109] Yonenaga, I., A. Matsui, S. Tozawa, K. Sumino, and T. Fukuda. Czochralski growth of Ge1-xSix alloy crystals. Journal of Crystal Growth, Vol. 154, No. 3-4, 1995, pp. 275-279.
- Matsui, A., I. Yonenaga, and K. Sumino. Czochralski growth of [110] bulk crystals of Ge1-xSix alloys. Journal of Crystal Growth, Vol. 183, No. 1-2, 1998, pp. 109-116.
- [111] Yonenaga, I. and M. Nonaka. Czochralski growth of bulk crystals of $Ge_{1-x}Si_x$ alloys: II. Si-rich alloys. Journal of Crystal Growth, Vol. 191, No. 3, 1998, pp. 393-398.
- Yonenaga, I. Czochralski growth of GeSi bulk alloy crystals. Journal [112] of Crystal Growth, Vol. 198, 1999, pp. 404-408.
- Yonenaga, I. Czochralski growth of heavily impurity doped crystals of GeSi alloys. Journal of Crystal Growth, Vol. 226, No. 1, 2001, pp. 47-51.
- Yonenaga, I. Growth and fundamental properties of SiGe bulk crystals. Journal of Crystal Growth, Vol. 275, No. 1-2, 2005, pp. 91-98.
- Tiller, W. A., K. A. Jackson, J. W. Rutter, and B. Chalmers. The redistribution of solute atoms during the solidification of metals. Acta Metallurgica, Vol. 1, No. 4, 1953, pp. 428-437.
- Agnieszka, T., L. L. Chun, C. H. Hung, H. L. Jhen, K. J. Ming, I. H. Po, et al. Shape of Ni-containing nanoislands grown on an Ag-terminated Ge(111) surface. Surface & Coatings Technology, Vol. 398, 2020, id. 126079.
- Mohamed, H. F., C. Xia, Q. Sai, H. Cui, M. Pan, and H. Qi. Growth and fundamentals of bulk β-Ga₂O₃ single crystals. *Journal of* Semiconductors, Vol. 40, No. 1, 2019, id. 011801.
- Deitch, R. H., S. H. Jones, and T. G. Digges. Bulk single crystal growth of silicon-germanium. Journal of Electronic Materials, Vol. l29, No. 9, 2000, pp. 1074-1078.
- [119] Abrosimov, N. V., S. N. Rossolenko, W. Thieme, A. Gerhardt, and W. Schröder. Czochralski growth of Si-and Ge-rich SiGe single crystals. Journal of Crystal Growth, Vol. 174, No. 1-4, 1997,
- [120] Wei, Q., M. Mukaida, K. Kirihara, Y. Naitoh, and T. Ishida. Recent progress on PEDOT-based thermoelectric materials. Materials, Vol. 8, 2015, pp. 732-750.
- [121] Bubnova, O., Z. U. Khan, A. Malti, S. Braun, M. Fahlman, M. Berggren, et al. Optimization of the thermoelectric figure of merit in the conducting polymer poly(3,4-ethylenedioxythiophene). Nature Materials, Vol. 10, 2011, id. 429.
- Asano, H., N. Sakura, K. Oshima, Y. Shiraishi, and N. Toshima. Development of ethenetetrathiolate hybrid thermoelectric

- materials consisting of cellulose acetate and semiconductor nanomaterials. Japanese Journal of Applied Physics, Vol. 55, 2016, id. 02BB02.
- [123] Gayner, C. and K. K. Kar. Recent advances in thermoelectric materials. Progress in Materials Science, Vol. 83, 2016, pp. 330-382.
- Ferrari, A. C., F. Bonaccorso, V. Fal'ko, K. S. Novoselov, S. Roche, P. Bøggild, et al. Science and technology roadmap for graphene, related two-dimensional crystals, and hybrid systems. Nanoscale, Vol. 7, 2015, pp. 4598-4810.
- [125] Zong, P., J. Liang, P. Zhang, C. Wan, Y. Wang, and K. Koumoto. Graphene-based thermoelectrics. ACS Applied Energy Materials, Vol. 3, 2020, pp. 2224-2239.
- [126] Sankeshwar, N. S., S. S. Kubakaddi, and B. G. Mulimani. Advances in graphene science, Vol. 9, A. Mahmood, Ed., IntechOpen, Rijeka, 2013, pp. 217-271.
- [127] Burton, R., S. Mehraban, D. Beynon, J. McGettrick, T. Watson, N. P. Lavery, et al. 3D printed SnSe thermoelectric generators with high figure of merit. Advanced Energy Materials, Vol. 9, 2019,
- [128] Usami, N. Types of silicon-germanium (SiGe) bulk crystal growth methods and their applications. In Silicon-Germanium (SiGe) Nanostructures, Woodhead Publishing, Tohoku University, Japan, 2011, pp. 72-82.
- [129] Hicks, L. D. and M. S. Dresselhaus. Thermoelectric figure of merit of a one-dimensional conductor. Physical Review B, Condensed Matter, Vol. 47, No. 24, 1993, pp. 16631-16634.
- [130] Yang, J. and T. Caillat. Thermoelectric materials for space and automotive power generation. MRS Bulletin, Vol. 31, No. 3, 2006, pp. 224-229.
- [131] Hicks, L. D. and M. S. Dresselhaus. Effect of quantum-well structures on the thermoelectric figure of merit. Physical Review B, Condensed Matter, Vol. 47, No. 19, 1993, pp. 12727-12731.
- Lv, H. Y., H. J. Liu, J. Shi, X. F. Tang, and C. Uher. Optimized thermoelectric performance of Bi₂Te₃ nanowires. Journal of Materials Chemistry A: Materials for Energy and Sustainability, Vol. 1, No. 23, 2013, pp. 6831-6838.
- [133] Wei, J., L. Yang, Z. Ma, P. Song, M. Zhang, J. Ma, et al. Review of current high-ZT thermoelectric materials. Journal of Materials Science, Vol. 55, 2020, pp. 12642-12704.
- [134] Wu, F., H. Song, J. Jia, and X. Hu. Effects of Ce, Y, and Sm doping on the thermoelectric properties of Bi₂Te₃ alloy. *Progress in Natural* Science: Materials International, Vol. 23, No. 4, 2013, pp. 408-412.
- [135] Wu, F., W. Wang, X. Hu, and M. Tang. Thermoelectric properties of I-doped n-type Bi₂Te₃-based material prepared by hydrothermal and subsequent hot pressing. Progress in Natural Science: Materials International, Vol. 27, No. 2, 2017, pp. 203-207.
- Lee, G. E., I. H. Kim, Y. S. Lim, W. S. Seo, B. J. Choi, and C. W. [136] Hwang. Preparation and thermoelectric properties of doped Bi₂Te₃-Bi₂Se₃ solid solutions. *Journal of Electronic Materials*, Vol. 43, 2014, pp. 1650-1655.
- Lee, J. U., D. H. Lee, B. Kwon, D. B. Hyun, S. Nahm, S. H. Baek, et al. [137] Effect of sn doping on the thermoelectric properties of n-type Bi₂(Te, Se)₃ alloys. Journal of Electronic Materials, Vol. 44, 2015, pp. 1926-1930.
- [138] Wu, Y., R. Zhai, T. Zhu, and X. Zhao. Enhancing room temperature thermoelectric performance of n-type polycrystalline bismuthtelluride-based alloys via Ag doping and hot deformation. Materials Today Physics, Vol. 2, 2017, pp. 62-68.
- Soni, A., Z. Yanyuan, Y. Ligen, M. K. K. Aik, M. S. Dresselhaus, and Q. Xiong. Enhanced thermoelectric properties of solution grown

- Bi₂Te_{3-x}Se_x nanoplatelet composites. *Nano Letters*, Vol. 12, No. 3, 2012, pp. 1203-1209.
- [140] Zhou, Y., L. Li, Q. Tan, and J. F. Li. Thermoelectric properties of Pbdoped bismuth telluride thin films deposited by magnetron sputtering. Journal of Alloys and Compounds, Vol. 590, 2014, pp. 362-367.

DE GRUYTER

- [141] Wu, F., Q. He, M. Tang, and H. Song. Thermoelectric properties of Tl and I dual-doped Bi₂Te₃-based alloys. International Journal of Modern Physics B, Vol. 32, No. 10, 2018, id. 1850123.
- [142] Singh, A., P. Shahi, A. K. Ghosh, J. G. Cheng, and S. Chatterjee. Enhancement in power factor due to anti-correlation between electrical conductivity and thermoelectric power and induced magnetic ordering in high mobility Zn doped Bi₂Te₃ topological insulator. Journal of Alloys and Compounds, Vol. 731, 2018, pp. 297-302.
- [143] Arif, F., O. Faroog, Z. F. Tuz, and M. Anis-ur-Rehman. Structural and thermoelectric properties of Gd doped Bi₂Te₃. Key Engineering Materials, Vol. 778, 2018, pp. 189-194.
- [144] Sun, T., M. K. Samani, N. Khosravian, K. M. Ang, Q. Yan, B. K. Tay, et al. Enhanced thermoelectric properties of n-type Bi₂Te_{2, 7}Se_{0,3} thin films through the introduction of Pt nanoinclusions by pulsed laser deposition. Nano Energy, Vol. 8, 2014, pp. 223-230.
- [145] Wu, H. J., B. Y. Chen, and H. Y. Cheng. The pn conduction type transition in Ge-incorporated Bi₂Te₃ thermoelectric materials. Acta Materialia, Vol. 122, 2017, pp. 120-129.
- [146] Li, A. H., M. Shahbazi, S. H. Zhou, G. X. Wang, C. Zhang, P. Jood, et al. Electronic structure and thermoelectric properties of Bi₂Te₃ crystals and graphene-doped Bi₂Te₃. *Thin Solid Films*, Vol. 518, No. 24, 2010, pp. e57-e60.
- [147] Ju, H. and J. Kim. Preparation and structure dependent thermoelectric properties of nanostructured bulk bismuth telluride with graphene. Journal of Alloys and Compounds, Vol. 664, 2016, pp. 639-647.
- [148] Ju, H., M. Kim, and J. Kim. A facile fabrication of n-type Bi₂Te₃ nanowire/graphene layer-by-layer hybrid structures and their improved thermoelectric performance. Chemical Engineering Journal, Vol. 275, 2015, pp. 102-112.
- Hummers, W. S. and R. E. Offeman. Preparation of graphitic oxide. Journal of the American Chemical Society, Vol. 80, No. 6, 1958, pp. 1339-1339.
- [150] Yitong, G., D. Jingyang, H. Meihua, W. Bin, S. Taichao, and Z. Aiguo. Improve thermoelectric performance of Bi₂Te₃ by incorporation of Mo₂C MXene with N-type conductivity. Journal of Materials Science: Materials in Electronics, Vol. 34, 2023, id. 685.
- [151] Agarwal, K., V. Kaushik, D. Varandani, A. Dhar, and B. R. Mehta. Nanoscale thermoelectric properties of Bi₂Te₃-Graphene nanocomposites: Conducting atomic force, scanning thermal and kelvin probe microscopy studies. Journal of Alloys and Compounds, Vol. 681, 2016, pp. 394-401.
- [152] Vijaya Shanthi, R., K. Neyvasagam, R. Kayalvizhi, and M. John Abel. MgO nanoparticles with altered structural and optical properties by doping (Er³⁺) rare earth element for improved photocatalytic activity. Applied Physics A, Vol. 128, 2022, id. 133.
- [153] Cham, K., C. Jaehun, K. Taewook, and H. L. David. Interfacial effects in an inorganic/organic composite based on Bi₂Te₃ inducing decoupled transport properties and enhanced thermoelectric performance. Journal of Materials Chemistry A, Vol. 10, 2022, pp. 13780-13792.
- Snyder, G. J. and E. S. Toberer. Complex thermoelectric materials. Nature Materials, Vol. 7, No. 2, 2008, pp. 105-114.

- [155] Bhatia, M. L. Volume of formation and ligand field effects in some intermetallics. Intermetallics, Vol. 7, No. 6, 1999, pp. 641-651.
- [156] Sahiba, B., P. Ying, A. Takashi, C. Raju, and M. Takao. Realizing enhanced thermoelectric performance in n-type Mg₃(Bi,Sb)₂based film. Journal of Materials Chemistry C, Vol. 11, 2023, pp. 15130-15137.
- Weigiang, W., D. Zhenhong, W. Xichang, Z. Qi, Z. Yinchang, and M. [157] Sheng. Low lattice thermal conductivity and high figure of merit in n-type doped full-Heusler compounds X_2YAu (X = Sr, Ba; Y = as, Sb). International Journal of Energy Research, Vol. 45, No. 15, 2021, pp. 20949-20958.
- [158] Liu, W. S., Q. Zhang, Y. Lan, S. Chen, X. Yan, Q. Zhang, et al. Thermoelectric property studies on Cu-doped n-type CuxBi₂Te_{2.7}Se_{0.3} nanocomposites. *Advanced Energy Materials*, Vol. 1, No. 4, 2011, pp. 577-587.
- [159] Zhang, Y. H., T. J. Zhu, J. P. Tu, and X. B. Zhao. Flower-like nanostructure and thermoelectric properties of hydrothermally synthesized La-containing Bi₂Te₃ based alloys. Materials Chemistry and Physics, Vol. 103, No. 2-3, 2007, pp. 484-488.
- [160] Wu, F., H. Song, J. Jia, and X. Hu. Effects of Ce, Y, and Sm doping on the thermoelectric properties of Bi₂Te₃ alloy. Progress in Natural Science: Materials International, Vol. 23, No. 4, 2013, pp. 408-412.
- Yan, X., B. Poudel, Y. Ma, W. S. Liu, G. Joshi, H. Wang, et al. [161] Experimental studies on anisotropic thermoelectric properties and structures of n-type Bi₂Te_{2,7}Se_{0,3}. Nano Letters, Vol. 10, No. 9, 2010, pp. 3373-3378.
- [162] Wu, F., W. Wang, X. Hu, and M. Tang. Thermoelectric properties of I-doped n-type Bi₂Te₃-based material prepared by hydrothermal and subsequent hot pressing. Progress in Natural Science: Materials International, Vol. 27, No. 2, 2017, pp. 203-207.
- [163] Wu, F., H. Song, F. Gao, W. Shi, J. Jia, and X. Hu. Effects of different morphologies of Bi₂Te₃ nanopowders on thermoelectric properties. Journal of Electronic Materials, Vol. 42, 2013, pp. 1140-1145.
- Γ1641 Shi, W., F. Wu, K. Wang, J. Yang, H. Song, and X. Hu. Preparation and thermoelectric properties of yttrium-doped Bi₂Te₃ flower-like nanopowders. Journal of Electronic Materials, Vol. 43, 2014, pp. 3162-3168.
- Yang, J., F. Wu, Z. Zhu, L. Yao, H. Song, and X. Hu. Thermoelectrical [165] properties of lutetium-doped Bi₂Te₃ bulk samples prepared from flower-like nano-powders. Journal of Alloys and Compounds, Vol. 619, 2015, pp. 401-405.
- [166] Wu, F., W. Shi, and X. Hu. Preparation and thermoelectric properties of flower-like nanoparticles of Ce-Doped Bi₂Te₃. Electronic Materials Letters, Vol. 11, 2015, pp. 127-132.
- [167] Liu, W., X. Yan, G. Chen, and Z. Ren. Recent advances in thermoelectric nanocomposites. Nano Energy, Vol. 1, No. 1, 2012, pp. 42-56.
- Wang, S., W. Xie, H. Li, and X. Tang. Enhanced performances [168] of melt spun Bi₂(Te, Se)₃ for n-type thermoelectric legs. Intermetallics, Vol. 19, No. 7, 2011, pp. 1024-1031.
- Tritt, T. M. Holey and unholey semiconductors. Science, Vol. 283, [169] No. 5403, 1999, pp. 804-805.
- Liu, W. S., Q. Zhang, Y. Lan, S. Chen, X. Yan, Q. Zhang, et al. [170] Thermoelectric property studies on Cu-doped n-type CuxBi₂Te_{2.7}Se_{0.3} nanocomposites. Advanced Energy Materials, Vol. 1, No. 4, 2011, pp. 577-587.
- Lan, Y., A. J. Minnich, G. Chen, and Z. Ren. Enhancement of thermoelectric figure-of-merit by a bulk nanostructuring approach. Advanced Functional Materials, Vol. 20, No. 3, 2010, pp. 357-376.

- [172] Jiang, J., L. Chen, Q. Yao, S. Bai, and Q. Wang. Effect of TeI4 content on the thermoelectric properties of n-type Bi-Te-Se crystals prepared by zone melting. *Materials Chemistry and Physics*, Vol. 92, No. 1, 2005, pp. 39–42.
- [173] Cui, J. L., L. D. Mao, W. Yang, X. B. Xu, D. Y. Chen, and W. J. Xiu. Thermoelectric properties of Cu-doped n-type (Bi_2Te_3) $0.9-(Bi_2-_xCu_xSe_3)$ 0.1 (x = 0-0.2) alloys. *Journal of Solid State Chemistry*, Vol. 180, No. 12, 2007, pp. 3583-3587.
- [174] Zhang, X., X. Y. Ma, Q. M. Lu, F. P. Zhang, Y. Q. Liu, J. X. Zhang, et al. Thermoelectric properties of Ag-doped n-type (Bi _{2-x} Ag _x Te ₃) 0.96-(Bi ₂ Se ₃) 0.04 Pseudobinary alloys. *Journal of Electronic Materials*, Vol. 40, 2011, pp. 773-777.
- [175] Rowe, D. M., (Ed.), CRC handbook of thermoelectrics, CRC Press, Boca Raton. FL. 1995.
- [176] Poudel, B., Q. Hao, Y. Ma, Y. Lan, A. Minnich, B. Yu, et al. High-thermoelectric performance of nanostructured bismuth anti-mony telluride bulk alloys. *Science*, Vol. 320, No. 5876, 2008, pp. 634–638.
- [177] Hu, L., H. Wu, T. Zhu, C. Fu, J. He, P. Ying, et al. Tuning multiscale microstructures to enhance thermoelectric performance of n-type Bismuth-Telluride-based solid solutions. *Advanced Energy Materials*, Vol. 5, No. 17, 2015, id. 1500411.
- [178] Kim, S. I., K. H. Lee, H. A. Mun, H. S. Kim, S. W. Hwang, J. W. Roh, et al. Dense dislocation arrays embedded in grain boundaries for high-performance bulk thermoelectrics. *Science*, Vol. 348, No. 6230, 2015, pp. 109–114.
- [179] Tang, X., W. Xie, H. Li, W. Zhao, Q. Zhang, and M. Niino.

 Preparation and thermoelectric transport properties of highperformance p-type Bi₂Te₃ with layered nanostructure. *Applied Physics Letters*, Vol. 90, No. 1, 2007, id. 012102.
- [180] Cao, Y. Q., X. B. Zhao, T. J. Zhu, X. B. Zhang, and J. P. Tu. Syntheses and thermoelectric properties of Bi₂Te₃/ Sb₂Te₃ bulk nanocomposites with laminated nanostructure. *Applied Physics Letters*, Vol. 92, No. 14, 2008, id. 143106.
- [181] Mehta, R. J., Y. Zhang, C. Karthik, B. Singh, R. W. Siegel, T. T. Borca, et al. A new class of doped nanobulk high-figure-of-merit thermoelectrics by scalable bottom-up assembly. *Nature Materials*, Vol. 11, No. 3, 2012, pp. 233–240.
- [182] Shen, J. J., T. J. Zhu, X. B. Zhao, S. N. Zhang, S. H. Yang, and Z. Z. Yin. Recrystallization induced in situ nanostructures in bulk bismuth antimony tellurides: a simple top down route and improved thermoelectric properties. *Energy & Environmental Science*, Vol. 3, No. 10, 2010, pp. 1519–1523.
- [183] Hu, L. P., T. J. Zhu, Y. G. Wang, H. H. Xie, Z. J. Xu, and X. B. Zhao. Shifting up the optimum figure of merit of p-type bismuth telluride-based thermoelectric materials for power generation by suppressing intrinsic conduction. NPG Asia Materials, Vol. 6, No. 2, 2014, id. e88.
- [184] Xu, Z., H. Wu, T. Zhu, C. Fu, X. Liu, L. Hu, et al. Attaining high midtemperature performance in (Bi, Sb)₂Te₃ thermoelectric materials via synergistic optimization. NPG Asia Materials, Vol. 8, No. 9, 2016, id. e302.
- [185] An, Z., J. S. Li, and Y. Feng. Microstructure evolution of a new nearβ titanium alloy: Ti555211 during high-temperature deformation. *Rare Metals*, Vol. 34, 2015, pp. 757–763.
- [186] Hou, X. L., Y. Li, P. Lv, J. Cai, L. Ji, and Q. F. Guan. Hot deformation behavior and microstructure evolution of a Mg–Gd–Nd–Y–Zn alloy. *Rare Metals*, Vol. 35, 2016, pp. 532–536.
- [187] Yan, X., B. Poudel, Y. Ma, W. S. Liu, G. Joshi, H. Wang, et al. Experimental studies on anisotropic thermoelectric properties

- and structures of n-type $Bi_2Te_{2.7}Se_{0.3}$. Nano Letters, Vol. 10, No. 9, 2010, pp. 3373–3378.
- [188] Liu, W. S., Q. Zhang, Y. Lan, S. Chen, X. Yan, Q. Zhang, et al. Thermoelectric property studies on Cu-doped n-type CuxBi₂Te_{2.} ₇Se_{0. 3} nanocomposites. *Advanced Energy Materials*, Vol. 1, No. 4, 2011, pp. 577–587.
- [189] Lotgering, F. K. Topotactical reactions with ferrimagnetic oxides having hexagonal crystal structures – I. Journal of Inorganic and Nuclear Chemistry, Vol. 9, No. 2, 1959, pp. 113–123.
- [190] Süssmann, H., A. Priemuth, and U. Pröhl. Doping properties of Pb and Ge in Bi₂Te₂ and Sb₂Te₃. *Physica Status Solidi (a)*, Vol. 82, No. 2, 1984, pp. 561–567.
- [191] Plecháček, T., J. Navrátil, J. Horák, D. Bachan, A. Krejčová, and P. Lošťák. Point and structural defects in Bi₂Pb_xTe₃ single crystals. Solid State Ionics, Vol. 177, No. 39–40, 2007, pp. 3513–3519.
- [192] Kim, D. H., E. Byon, G. H. Lee, and S. Cho. Effect of deposition temperature on the structural and thermoelectric properties of bismuth telluride thin films grown by co-sputtering. *Thin Solid Films*, Vol. 510, No. 1–2, 2006, pp. 148–153.
- [193] Jeon, S. J., M. Oh, H. Jeon, S. Hyun, and H. J. Lee. Effects of postannealing on thermoelectric properties of bismuth–tellurium thin films deposited by co-sputtering. *Microelectronic Engineering*, Vol. 88, No. 5, 2011, pp. 541–544.
- [194] Deng, Y., H. M. Liang, Y. Wang, Z. W. Zhang, M. Tan, and J. L. Cui. Growth and transport properties of oriented bismuth telluride films. *Journal of Alloys and Compounds*, Vol. 509, No. 18, 2011, pp. 5683–5687.
- [195] Lee, H. J., H. S. Park, S. Han, and J. Y. Kim. Thermoelectric properties of n-type Bi–Te thin films with deposition conditions using RF magnetron co-sputtering. *Thermochimica Acta*, Vol. 542, 2012, pp. 57–61.
- [196] Hasan, M. Z. and C. L. Kane. Colloquium: topological insulators. Reviews of Modern Physics, Vol. 82, No. 4, 2010, id. 3045.
- [197] Fu, L. and C. L. Kane. Probing neutral Majorana fermion edge modes with charge transport. *Physical Review Letters*, Vol. 102, No. 21, 2009, id. 216403.
- [198] Wray, L. A., S. Y. Xu, Y. Xia, Y. S. Hor, D. Qian, A. V. Fedorov, et al. Observation of topological order in a superconducting doped topological insulator. *Nature Physics*, Vol. 6, No. 11, 2010, pp. 855–859.
- [199] Hor, Y. S., A. J. Williams, J. G. Checkelsky, P. Roushan, J. Seo, Q. Xu, et al. Superconductivity in Cu_xBi₂Se₃ and its implications for pairing in the undoped topological insulator. *Physical Review Letters*, Vol. 104, No. 5, 2010, id. 057001.
- [200] Qi, X. L. and S. C. Zhang. Topological insulators and superconductors. *Reviews of Modern Physics*, Vol. 83, No. 4, 2011, id. 1057.
- [201] Roushan, P., J. Seo, C. V. Parker, Y. S. Hor, D. Hsieh, D. Qian, et al. Topological surface states protected from backscattering by chiral spin texture. *Nature*, Vol. 460, No. 7259, 2009, pp. 1106–1109.
- [202] Seradjeh, B., J. E. Moore, and M. Franz. Exciton condensation and charge fractionalization in a topological insulator film. *Physical Review Letters*, Vol. 103, No. 6, 2009, id. 066402.
- [203] Qi, X. L., R. Li, J. Zang, and S. C. Zhang. Inducing a magnetic monopole with topological surface states. *Science*, Vol. 323, No. 5918, 2009, pp. 1184–1187.
- [204] Yu, R., W. Zhang, H. J. Zhang, S. C. Zhang, X. Dai, and Z. Fang. Quantized anomalous Hall effect in magnetic topological insulators. *Science*, Vol. 329, No. 5987, 2010, pp. 61–64.

- [205] Checkelsky, J. G., Y. S. Hor, R. J. Cava, and N. P. Ong. Bulk band gap and surface state conduction observed in voltage-tuned crystals of the topological insulator Bi₂Se₃. *Physical Review Letters*, Vol. 106, No. 19, 2011, id. 196801.
- [206] He, H. T., G. Wang, T. Zhang, I. K. Sou, G. K. Wong, J. N. Wang, et al. Impurity effect on weak antilocalization in the topological insulator Bi₂Te₃. *Physical Review Letters*, Vol. 106, No. 16, 2011, id. 166805.
- [207] Chen, J., H. J. Qin, F. Yang, J. Liu, T. Guan, F. M. Qu, et al. Gate-voltage control of chemical potential and weak antilocalization in Bi₂Se₃. *Physical Review Letters*, Vol. 105, No. 17, 2010, id. 176602.
- [208] Peng, H., K. Lai, D. Kong, S. Meister, Y. Chen, X. L. Qi, et al. Aharonov–Bohm interference in topological insulator nanoribbons. *Nature Materials*, Vol. 9, No. 3, 2010, pp. 225–229.
- [209] Checkelsky, J. G., Y. S. Hor, M. H. Liu, D. X. Qu, R. J. Cava, and N. P. Ong. Quantum interference in macroscopic crystals of nonmetallic Bi₂Se₃. *Physical Review Letters*, Vol. 103, No. 24, 2009, id. 246601
- [210] Novoselov, K. S., A. K. Geim, S. V. Morozov, D. E. Jiang, Y. Zhang, S. V. Dubonos, et al. Electric field effect in atomically thin carbon films. *Science*, Vol. 306, No. 5696, 2004, pp. 666–669.
- [211] Novoselov, K. S., A. K. Geim, S. V. Morozov, D. E. Jiang, Y. Zhang, S. V. Dubonos, et al. Electric field effect in atomically thin carbon films. *Science*, Vol. 306, No. 5696, 2004, pp. 666–669.
- [212] Zebarjadi, M., K. Esfarjani, M. S. Dresselhaus, Z. F. Ren, and G. Chen. Perspectives on thermoelectrics: from fundamentals to device applications. *Energy & Environmental Science*, Vol. 5, No. 1, 2012, pp. 5147–5162.
- [213] Kishi, M., H. Nemoto, T. Hamao, M. Yamamoto, S. Sudou, M. Mandai, et al. Micro thermoelectric modules and their application to wristwatches as an energy source. In *Eighteenth International Conference on Thermoelectrics. Proceedings, ICT'99* (Cat. No. 99TH8407) 1999, IEEE, 1999, August, pp. 301–307.
- [214] Rowe, D. M. CRC handbook of thermoelectrics, CRC Press, Boca Raton, New York, London, Tokyo, 1995.
- [215] Yazawa, K. and A. Shakouri. Cost-performance analysis and optimization of fuel-burning thermoelectric power generators. *Journal of Electronic Materials*, Vol. 42, 2013, pp. 1946–1950.
- [216] Department for Business Energy & Industrial Strategy, Electricity Generation Costs; 2016. https://www.gov.uk/government/publications/beiselectricity-generation-costs-november-2016 (accessed: September 2021).
- [217] Burton, M., G. Howells, J. Atoyo, and M. Carnie. Printed thermoelectrics. Advanced Materials, Vol. 34, No. 18, 2022, id. 2108183.
- [218] Ostfeld, A. E., I. Deckman, A. M. Gaikwad, C. M. Lochner, and A. C. Arias. Screen printed passive components for flexible power electronics. *Scientific Reports*, Vol. 5, No. 1, 2015, id. 15959.
- [219] Mariani, P., L. Vesce, and A. Di Carlo. The role of printing techniques for large-area dye sensitized solar cells. Semiconductor Science and Technology, Vol. 30, No. 10, 2015, id. 104003.
- [220] De Rossi, F., J. A. Baker, D. Beynon, K. E. A. Hooper, S. M. P. Meroni, et al. All printable perovskites solar modules with 198cm² active area and over 6% efficiency. Advanced Materials Technologies, Vol. 3, 2018, id. 1800156.
- [221] Raptis, D., V. Stoichkov, S. M. Meroni, A. Pockett, C. A. Worsley, M. Carnie, et al. Enhancing fully printable mesoscopic perovskite solar cell performance using integrated metallic grids to improve carbon electrode conductivity. *Current Applied Physics*, Vol. 20, No. 5, 2020, pp. 619–627.

- [222] Baker, J., K. Hooper, S. Meroni, A. Pockett, J. McGettrick, Z. Wei, et al. High throughput fabrication of mesoporous carbon perovskite solar cells. *Journal of Materials Chemistry A*, Vol. 5, No. 35, 2017, pp. 18643–18650.
- [223] Öhlund, T. Metal Films for Printed Electronics: Ink-substrate Interactions and Sintering, PhD Thesis, Kopieringen Mid Sweden University, Sundsvall, Sweden, 2014.
- [224] Kipphan, H. Handbook of print media: technologies and production methods, Springer-Verlag Berlin Heidelberg, 2001.
- [225] Weber, J., K. K. Potje, F. Haase, P. Detemple, F. Völklein, and T. Doll. Coin-size coiled-up polymer foil thermoelectric power generator for wearable electronics. Sensors and Actuators, A: Physical, Vol. 132, No. 1, 2006, pp. 325–330.
- [226] Cao, Z., E. Koukharenko, M. J. Tudor, R. N. Torah, and S. P. Beeby. Screen printed flexible Bi₂Te₃-Sb₂Te₃ based thermoelectric generator. In *Journal of Physics: Conference Series 2013*, Vol. 476, 2013, December.
- [227] Le, H. P. Progress and trends in ink-jet printing technology. Journal of Imaging Science and Technology, Vol. 42, No. 1, 1998, pp. 49–62.
- [228] Wooik, J., H. J. Yoon, V. P. Peter, F. Jicheng, Y. Younghwan, K. Minkyung, et al. Three-dimensional nanoprinting via charged aerosol jets. *Nature*, Vol. 592, 2021, pp. 54–59.
- [229] Sarbajna, A., A. G. Rösch, L. Franke, U. Lemmer, and M. M. Mallick. Inorganic-based printed thermoelectric materials and devices. Advanced Engineering Materials, Vol. 25, No. 2, 2023, id. 2200980.
- [230] Ahmad, A. Z. and A. Ali. Design and construction of thermoelectric generator with comparison of sun and water heat temperatures. *IOP Conference Series: Earth and Environmental Science*, Vol. 1104, 2022, id. 012032.
- [231] Kim, S. J., J. H. We, and B. J. Cho. A wearable thermoelectric generator fabricated on a glass fabric. *Energy & Environmental Science*, Vol. 7, No. 6, 2014, pp. 1959–1965.
- [232] Rösch, A. G., A. Gall, S. Aslan, M. Hecht, L. Franke, M. M. Mallick, et al. Fully printed origami thermoelectric generators for energyharvesting. npj Flexible. *Electronics*, Vol. 5, No. 1, 2021, id. 1.
- [233] We, J. H., S. J. Kim, and B. J. Cho. Hybrid composite of screenprinted inorganic thermoelectric film and organic conducting polymer for flexible thermoelectric power generator. *Energy*, Vol. 73, 2014, pp. 506–512.
- [234] Kato, K., K. Kuriyama, T. Yabuki, and K. Miyazaki. Organic-inor-ganic thermoelectric material for a printed generator. *Journal of Physics: Conference Series*, Vol. 1052, 2018, id. 012008.
- [235] Pires, A. L., I. F. Cruz, J. Silva, G. N. Oliveira, T. S. Ferreira, A. M. Lopes, et al. Printed flexible μ-thermoelectric device based on hybrid Bi₂Te₃/PVA composites. ACS Applied Materials & Interfaces, Vol. 11, No. 9, 2019, pp. 8969–8981.
- [236] Saeidi, J. M., W. Kuang, C. Dun, and Y. Zhang. 3D conformal printing and photonic sintering of high-performance flexible thermoelectric films using 2D nanoplates. Advanced Functional Materials, Vol. 29, No. 35, 2019, id. 1901930.
- [237] Varghese, T., C. Dun, N. Kempf, J. M. Saeidi, C. Karthik, J. Richardson, et al. Flexible thermoelectric devices of ultrahigh power factor by scalable printing and interface engineering. Advanced Functional Materials, Vol. 30, No. 5, 2020, id. 1905796.
- [238] Ding, D., F. Sun, F. Xia, and Z. Tang. A high-performance and flexible thermoelectric generator based on the solution-processed composites of reduced graphene oxide nanosheets and bismuth telluride nanoplates. *Nanoscale Advances*, Vol. 2, No. 8, 2020, pp. 3244–3251.

- [239] Chen, A., D. Madan, P. K. Wright, and J. W. Evans. Dispenser-printed planar thick-film thermoelectric energy generators. *Journal of Micromechanics and Micro Engineering*, Vol. 21, No. 10, 2011, id. 104006.
- [240] Madan, D., Z. Wang, A. Chen, R. C. Juang, J. Keist, P. K. Wright, et al. Enhanced performance of dispenser printed MA n-type Bi₂Te₃ composite thermoelectric generators. ACS Applied Materials & Interfaces, Vol. 4, No. 11, 2012, pp. 6117–6124.
- [241] Varghese, T., C. Hollar, J. Richardson, N. Kempf, C. Han, P. Gamarachchi, et al. High-performance and flexible thermoelectric films by screen printing solution-processed nanoplate crystals. *Scientific Reports*, Vol. 6, No. 1, 2016, id. 33135.
- [242] Hou, W., X. Nie, W. Zhao, H. Zhou, X. Mu, W. Zhu, et al. Fabrication and excellent performances of Bi_{0.5}Sb_{1.5}Te₃/epoxy flexible thermoelectric cooling devices. *Nano Energy*, Vol. 50, 2018, pp. 766–776.
- [243] Wang, T., M. A. Roberts, I. A. Kinloch, and B. Derby. Inkjet printed carbon nanotube networks: the influence of drop spacing and drying on electrical properties. *Journal of Physics D: Applied Physics*, Vol. 45, No. 31, 2012, id. 315304.
- [244] Tortorich, R. P., E. Song, and J. W. Choi. Inkjet-printed carbon nanotube electrodes with low sheet resistance for electrochemical sensor applications. *Journal of the Electrochemical Society*, Vol. 161, No. 2, 2013, id. B3044.
- [245] Azoubel, S., S. Shemesh, and S. Magdassi. Flexible electroluminescent device with inkjet-printed carbon nanotube electrodes. *Nanotechnology*, Vol. 23, No. 34, 2012, id. 344003.
- [246] Horike, S., T. Fukushima, T. Saito, T. Kuchimura, Y. Koshiba, M. Morimoto, et al. Highly stable n-type thermoelectric materials fabricated via electron doping into inkjet-printed carbon nanotubes using oxygen-abundant simple polymers. *Molecular Systems Design & Engineering*, Vol. 2, No. 5, 2017, pp. 616–623.
- [247] Horike, S., T. Fukushima, T. Saito, Y. Koshiba, and K. Ishida. Photoinduced charge-carrier modulation of inkjet-printed carbon

- nanotubes via poly (vinyl acetate) doping and dedoping for thermoelectric generators. *Chemical Physics Letters*, Vol. 691, 2018, pp. 219–223.
- [248] Lee, S., S. Kim, A. Pathak, A. Tripathi, T. Qiao, Y. Lee, et al. Recent progress in organic thermoelectric materials and devices. *Macromolecular Research*, Vol. 28, No. 6, 2020, pp. 531–552.
- [249] Yao, C. J., H. L. Zhang, and Q. Zhang. Recent progress in thermoelectric materials based on conjugated polymers. *Polymers*, Vol. 11, No. 1, 2019, id. 107.
- [250] Dubey, N. and M. Leclerc. Conducting polymers: Efficient thermoelectric materials. *Part B: Polym Phys*, Vol. 49, 2011, id. 467.
- [251] Gueye, M. N., A. Carella, V. J. Faure, R. Demadrille, and J. P. Simonato. Progress in understanding structure and transport properties of PEDOT-based materials: A critical review. *Progress in Materials Science*, Vol. 108, 2020, id. 100616.
- [252] Atoyo, J., M. R. Burton, J. McGettrick, and M. J. Carnie. Enhanced electrical conductivity and Seebeck coefficient in PEDOT: PSS via a two-step ionic liquid and NaBH₄ treatment for organic thermoelectrics. *Polymers*, Vol. 12, No. 3, 2020, id. 559.
- [253] Kim, J., J. G. Jang, J. I. Hong, S. H. Kim, and J. Kwk. Sulfuric acid vapor treatment for enhancing the thermoelectric properties of PEDOT: PSS thin-films. *Journal of Materials Science: Materials in Electronics*, Vol. 27, 2016, pp. 6122–6127.
- [254] Wang, X., F. Meng, H. Tang, Z. Gao, S. Li, F. Jiang, et al. An effective dual-solvent treatment for improving the thermoelectric property of PEDOT: PSS with white graphene. *Journal of Materials Science*, Vol. 52, 2017, pp. 9806–9818.
- [255] Worfolk, B. J., S. C. Andrews, S. Park, J. Reinspach, N. Liu, M. F. Toney, et al. Ultrahigh electrical conductivity in solution-sheared polymeric transparent films. *Proceedings of the National Academy of Sciences*, Vol. 112, No. 46, 2015, pp. 14138–14143.